Mechanical strength and band alignment of BAs/GaN heterojunction polar interfaces: A first-principles calculation study

Yuxi He and Hong Sun [*]

School of Physics and Astronomy, and Key Laboratory of Artificial Structures and Quantum Control (Ministry of Education), Shanghai Jiao Tong University, Shanghai 200240, China

(Received 23 September 2021; accepted 2 March 2022; published 21 March 2022)

Recently, GaN-on-BAs has been synthesized and demonstrated as a promising architecture for efficient thermal management in GaN based high-power electronic devices with remarkably reduced thermal boundary resistance compared to that of GaN-on-diamond. In this paper, we report studies on ideal strengths and band alignments for polar BAs/GaN heterojunctions and superlattices using first-principles calculations. The results show that under normal compression, all BAs/GaN interface configurations show much higher compressive stiffness compared to that in bulk GaN [0001] direction, with the GaN softening during its structural transformation under compression markedly suppressed, which improves protection of the electronic properties under external impacts. The natural band alignments of the mismatched BAs/GaN heterojunctions are calculated by a three-step approach. Most of the heterojunction and all the superlattice interfaces show type-II staggered band offsets. Large polarization built-in electric fields are predicated in superlattice with repeatedly positive- and negative-charged N-As and Ga-B interfaces, producing a saw-tooth like dipole potential, which can effectively separate electrons and holes to different interfaces, desirable for the photocatalytic processes. Our research shows that BAs/GaN heterojunction can not only provide a much-needed alternative to GaN-on-diamond heat dissipation system in future designing of high-power electronic devices, but also offers possibilities of applications in photovoltaic and photocatalytic devices as a type-II semiconductor heterojunction or superlattice.

DOI: 10.1103/PhysRevMaterials.6.034603

I. INTRODUCTION

Gallium nitride (GaN) based semiconductor materials enable numerous applications from efficient solar cells, solid-state lighting devices, to high-power and high-frequency transistors by virtue of its wide band gap, high electron saturation drift speed, high mechanical and thermal stability, high breakdown field, and capability of either n- or p-type doping [1–3]. Although the output power density in GaN based high-electron mobility transistors have been demonstrated to reach 40 ~ 50 W/mm [4,5], the heat dissipation of the self-heating channels become a severe bottleneck limiting these high-power electronic devices operating reliably under extreme high temperatures (600 ~ 700 °C in air or 1000 °C in vacuum) [6,7]. So far, GaN-on-SiC and GaN-on-diamond heterostructures are the available solutions to improve the thermal management in these GaN based high-power and high-frequency devices because of the large thermal conductivity of 4H-SiC (~450 W/mK) [8,9] and diamond (~2200 W/mK) [10,11]. However, inherent drawbacks exist in both of these substrate systems. In GaN-on-SiC systems, the relative moderate mismatch in crystal lattices (~3.7%) [12] and thermal expansion coefficients (~20.0%) [13–16] between GaN and SiC allotropes, such as 4H-SiC, makes it easy to grow GaN directly on SiC, which enables designing of the vertical conduction high-voltage and high-power devices to avoid degradation of electron mobility by interface quality and to increase its breakdown voltage by adjusting the thickness of SiC layer [17,18]. In addition, highly linear temperature sensors based on GaN/SiC heterojunction can be integrated directly on the same substrate of such GaN-on-SiC systems for accurate temperature monitoring under high-power operation [19]. However, the comparatively low thermal conductivity of 4H-SiC requires larger gate to gate spacing in GaN-on-Sic systems, and so reduces their areal power density [20]. In GaN-on-diamond systems, on the other hand, the high thermal conductivity of diamond substrate enables the reduction of gate pitches, which can increase the areal power density by at least 3 times [20]. But the large mismatch in crystal lattice (~11%) and thermal expansion coefficient (~86%) between GaN and diamond [15,21] makes it difficult to epitaxially grow GaN high quality single crystal film directly on diamond substrate with low thermal stresses. Moreover, the strong atomic bonding of diamond makes its phonon frequencies much higher than those in GaN and metal layers between GaN and diamond, which effectively increases phonon reflections on the interface and enhances the thermal boundary resistance between GaN self-heating channels and diamond substrate [22]. It is desirable to find new substrates, which possess not only the merits of both SiC and diamond, but also other advantages they do not have, that is, moderate mismatch in crystal lattices and thermal expansion coefficients, high thermal conductivity, and small

*hsun@sjtu.edu.cn

 ©2022 American Physical Society

thermal boundary resistance due to the maximum overlap of its phonon density of states with that of GaN. Boron arsenide (BAs), a III–V zinc-blende semiconductor recently synthesized in high quality with measured unusually high thermal conductivity (∼1300 W/mK) that surpasses all other bulk materials except diamond [23–25], prove particularly useful as a new substrate for thermal management and vertical operation of GaN based high-power devices [22] due to its relative moderate mismatch in crystal lattices (∼5.6%) [26] and thermal expansion coefficients (∼25%) [15] with GaN, comparable to those of 4H-SiC. More importantly, BAs also has a phonon density of states that overlaps perfectly with those of GaN and metal layers between GaN and BAs, which results in a reported eight-time reduction of thermal boundary resistance in a synthesized GaN-on-BAs system compared to that in GaN-on-diamond systems [22,27]. Furthermore, BAs has several other advantages compared to diamond, such as low costs and easy to adopt the existing III–V semiconductor technology [25]. With an indirect band gap structure similar to those of Si and 4H-SiC [28,29] and high optical absorption coefficient [30,31], BAs can also work as an active electronic and optoelectronic component, not merely a cooling substrate. Especially because BAs has both a high hole and electron mobility (2110 and 1400 cm^2/V s) [32] and native p-type dopability [33], together with its low mass density, low effective carrier mass, chemical stability at ambient conditions, it makes BAs an excellent material for versatile optoelectronic applications [32,34,35], including photocatalysis, photovoltaics, and photoelectronchemistry [31,32] etc. However, although high quality BAs crystals were successfully synthesized [23–25], due to the high volatility of arsenic, vacancy defects can be easily introduced during the synthesis of BAs, which can reduce their thermal conductivity, and as many arsenic compounds are toxic, extreme caution is required in experimental synthesis processes.

Recently, the applications of heterojunctions formed between group III-V and other semiconductors have attracted increasing attention, where the precise interface configurations and band alignments play a vital role. For instance, GaN can be used as a p-type semiconductor to form a GaN/ZnO heterojuction with n-type ZnO to design ultraviolet light-emitting diodes. Special polarization engineered N-polar p-GaN/O-polar n-ZnO interface greatly enhances the ultraviolet emission of the GaN/ZnO heterojunction [36], where the band alignment depends sensitively on interface configurations of the GaN/ZnO heterojunction [37]. Another example is BAs, of which the band gap (reduction), and electron and hole mobility (increase by 60%) can be controlled sensitively by strains resulted from the lattice mismatch of the heterostructure interfaces [26]. A $In_xGa_{1-x}N$/BAs heterostructure was proposed for photovoltaic device applications, and the calculation revealed a type-II band alignment with $0.3 < x < 1$, while a type-I band alignment was predicted for GaN/BAs ($x = 0$) [26], where the band alignments were obtained by calculating the average electrostatic potential inside each individual BAs and $In_xGa_{1-x}N$ slab to the vacuum region, and align the vacuum level of BAs and $In_xGa_{1-x}N$ to determine the band offsets. This method is simple as the detailed interface atomic configurations are neglected and is still being used by some authors [26,38,39]. However, if the detailed atomic interface configurations, including effects of polarizations and charge transformations between the interfaces are to be considered, the average electrostatic potential of the total interface structure is adopted to align the bands across the interface (see Sec. II), and this second method is more widely used [37,40–44]. Large differences in band alignments exist for different interface configurations when interface dipole and deformation potentials are included [45]. A typical example is the GaN/ZnO heterojunction, where a type-II band alignment was predicted but the conduction and valence band offset, (CBO and VBO), differ greatly for the Zn-N interface (CBO = 1.53 and VBO = 1.50 eV) and the Ga-O interface (CBO = 0.11 eV and VBO = 0.07 eV) [37]. This motivated us to carry out more detailed studies on BAs/GaN heterojunction with the interface configurations, interface dipole, and deformation potentials fully taken into consideration. Our results shown below that these effects make the band alignment of BAs/GaN heterojunction drastically different from those predicted previously [26]. The lattice constant (3.38 Å) of BAs on its (111) plane and that (3.19 Å) of GaN on its (0001) plane has a moderate mismatch of 5.6% in forming the BAs/GaN heterojunction, which is smaller than those of heterojunctions with large lattice mismatch (>7%) [46–49], but can still induce sharp in-plane strain deformation potential across the heterojunction interface [50]. For practical heterojunction applications, the exact conduction and valence band offsets are one of the most important quantities, which determine the confinement and transport property of carriers [51]. Effects of the atomic interfacial structures, interface polarizations and deformations, all can significantly change the band offsets between two semiconductors and alter the motion of charge carriers [43,52,53].

There exist three types of heterojunctions for applications in different fields. Most of electronic devices, such as optoelectronic light-emitting diodes, require a type-I band alignment to form quantum well heterostructures where CBO/VBO should be greater than 1 eV to confine electrons or holes competently [54,55]. While a type-II heterojunction can effectively reduce the recombination of electron-hole pairs to improve the photocatalytic efficiency, such as that in hydrogen generation from photocatalytic water splitting [56,57]. Recently, a superlattice structure with zincblende-wurtzite (ZB-WZ) interfaces has been proposed to spatially separate the photogenerated electrons and holes for efficient hydrogen generation from water splitting due to the type-II band alignment and the interface polarization-induced sawtooth-like electric field potential in the ZB-WZ superlattice [42]. In addition, such type-II band structure also facilitates the transport of charge carriers and dissociation of excitons, with potential applications in photovoltaic devices [58,59]. The charge carrier transport in a type-III heterojunction, where the band positions are further set off, can promote energy transition from conduction to valence bands, offering unique applications in tunnel field effect transistors and wavelength photodetectors [60,61]. Beyond that, the mechanical strength of the heterojunction interfaces should also receive special attention [62–64], as excessive compressive or cleavage stresses can lead to cracks that destabilize the heterojunction interfaces.

In this paper, we report in-depth studies on the mechanical strengths and band offsets in BAs/GaN heterojunctions

and superlattices. Four possible and energetically favorable microstructure interfaces of the BAs (111)/GaN (0001) heterojunction, selected from 12 tested configurations, are constructed using a large supercell with vacuum insertion on its two ends. The full-range stress-strain curves are calculated under tensile and compressive strains vertical to the BAs/GaN interface, which determine the cleavage and compression strengths of different interface configurations. A large enhancement of mechanical stiffness in the GaN parts of all the heterojunctions is observed and explained. The band alignment is investigated by the density functional theory (DFT) with the Heyd–Scuseria–Ernzerhof (HSE) hybrid functional, where the maximum positions of valence bands relative to (averaged) electrostatic potentials in the two bulk semiconductors, the dipole potential due to the difference between the electrostatic potentials of the two polar semiconductors forming the heterojunction, and the in-plane strain deformation potential across the interface are used to determine the VBO of the heterojunction (see more details below). Our calculations show that three out of the four BAs/GaN heterojunction interfaces, including the most stable B-N interface, show a type-II band alignment, different from the previous prediction, which can serve as a more appropriate starting point for studying tailored $In_xGa_{1-x}N$/BAs heterostructure with matched interface lattices [26]. We further show that in forming BAs/GaN superlattices, all the four interfaces become type-II band alignment. Especially, in BAs/GaN superlattices with periodical B-Ga and As-N interfaces, large interface polarization-induced saw-tooth like electric field potential exists, which can further separate electrons and holes into different interfaces, making the BAs/GaN superlattice structure particularly suitable for semiconductor photocatalytic applications.

II. COMPUTATIONAL DETAILS

A. First-principles calculations

First-principles calculations based on DFT are carried out with the electron-ion interaction described by the projector-augmented-wave (PAW) pseudopotentials [65], as implemented in the plane-wave basis code VASP [66,67], where the exchange-correlation interaction of electrons is treated by the generalized gradient approximation (GGA) proposed by Perdew–Burke–Ernzerhof (PBE) [68]. The unit cells of wurtzite GaN and zinc-blende BAs bulk structures are presented in Fig. 1, where the plane wave cutoff energy is set to 500 eV with a k-point mesh of $10 \times 10 \times 10$ and $10 \times 10 \times 6$ for BAs and GaN, respectively. Since the PBE functional will underestimate the band gap, the HSE hybrid functional [69,70] is adopted for the band gap calculation to achieve the values reported experimentally. The mixing parameter, α, describing the fractions of the short-range nonlocal Hartree-Fock and GGA exchanges [71,72], takes the value of 0.25 [26] and 0.35 [44] for BAs and GaN, respectively. For the structure optimization and electronic structure calculations, the convergence criteria of the total energy and Hellmann-Feynman force on atoms are set to 10^{-5} eV and 0.01 eV/Å. The calculated lattice parameters are listed in Table I below.

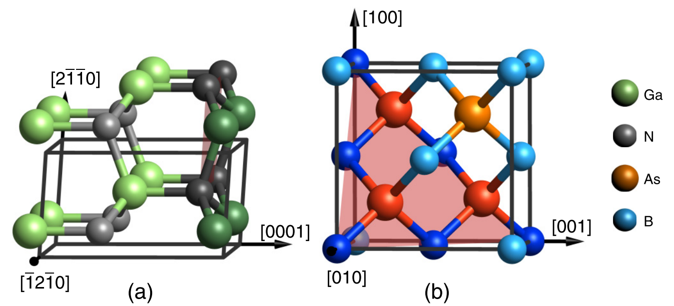

FIG. 1. The relaxed structures of (a) wurtzite GaN, (b) zinc-blende BAs bulk crystals, respectively. The species of atoms are indicated in the inset, where the darkened atoms represent those forming the bonding interface of the heterojunction.

B. Calculations of ideal strengths of heterojunctions

To study the mechanical properties of heterojunction interfaces, there exists two models: one is a periodical superlattice model, and the other is a slab model with vacuum insertion on its two ends. For the superlattice model, it generally involves two different kinds of interfaces [42,73,74]. The calculated mechanical properties of the superlattices, such as ideal tensile or compressive strength, are a reflection of the strengths for a composite material, instead of a single heterojunction, which cannot accurately describe the strength of one selected interface. In order to calculate the interfacial strength accurately for a selected interface configuration, we construct a heterojunction structure using the slab model. A slab supercell including 4 bilayer wurtzite (0001) plane of GaN and 3 trilayer zinc-blende (111) plane of BAs with a 40 Å vacuum on the two ends of the slab, which effectively separates different

TABLE I. The calculated lattice parameters (a, b, c) of bulk BAs and GaN, compared to other theoretical and experimental results, together with the obtained interface energy (γ_{IF}) and work of adhesion (W_{ad}) of the heterojunction with different interface bonding configurations.

Compounds	Lattice parameters (Å)					
	Present		Theory		Experiment	
	$a = b$	c	$a = b$	c	$a = b$	c
BAs	4.81	4.81	4.81	4.81 [82]	4.78	4.78 [24]
GaN	3.22	5.24	3.24	5.24 [83]	3.19	5.19 [84]
			3.21	5.26 [44]		
			3.19	5.19 [85]		

Heterojunction interface energy γ_{IF} (eV/Å^2)				
Interface bonding	1	2	3	4
γ_{IF}	0.069	0.164	0.092	0.202

Heterojunction interface work of adhesion W_{ad} (eV/Å^2)				
Interface bonding	1	2	3	4
W_{ad}	0.291	0.157	0.141	0.078

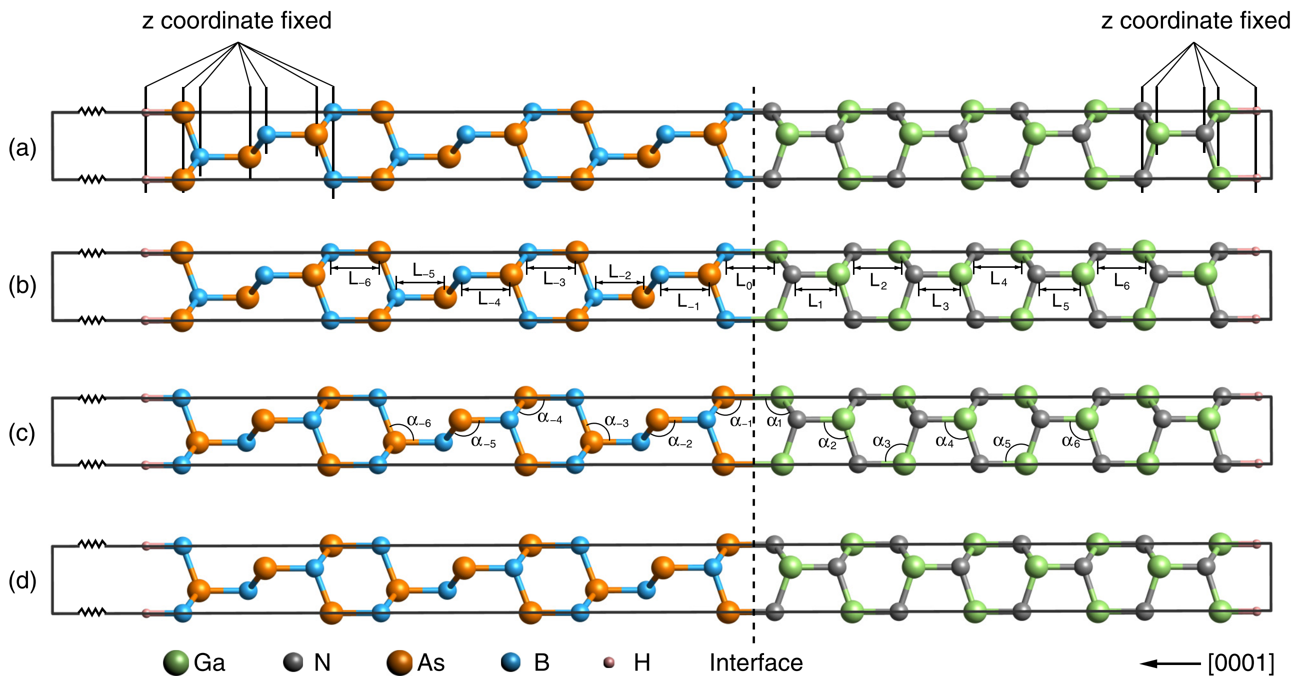

FIG. 2. The atomic structures of the polar BAs (111)/GaN (0001) heterojunction supercells, with an inserted 40 Å vacuum space (not fully shown), for (a) B-N (interface 1), (b) B-Ga (interface 2), (c) As-Ga (interface 3) and (d) As-N interface (interface 4). The species of atoms are indicated in the inset. The layer atoms with their z coordinates fixed during each step of the incrementally tensile or compressive deformations are indicated in (a).

slabs and avoid spurious periodical interactions, is used in the calculation as shown in Fig. 2. We select four B-N, B-Ga, As-Ga, and As-N interface configurations, assigned as interface "1-4", according to their heterojunction work of adhesion after complete relaxation of 12 tested interface equilibrium structures (see Fig. S1 and Table S1 in the Supplemental Material (SM) [75] for details). Passivation with pseudohydrogen is used to eliminate the surface states. The plane wave cutoff energy is set to 500 eV with a k-point mesh of $11 \times 11 \times 1$, which ensure the convergence of the energy and force on each atom in the heterojunction supercell to 10^{-5} eV and 0.01 eV/Å.

The uniaxial tensile or compressive loading are simulated by a quasistatic displacement-controlled deformation process similar to our previous calculations on indentation strength in bulk crystals with periodic nano-twinning interfaces [76,77], in which the lattice vectors of the supercell of the heterojunctions and the atomic slab thickness inside the supercell are incrementally deformed by applying tensile (or compressive) strains with an incremental strain step of $\delta\epsilon_{zz} = 0.005$ along the z direction normal to the heterojunction interfaces. At each step, the applied tensile strain ϵ_{zz}, and the z coordinates of one bottom bilayer of GaN and a top triple layer of BAs atoms [see Fig. 2(a)], are fixed to determine the calculated tensile stress σ_{zz}, while the other five independent components of the strain tensors and all the other atomic coordinates inside the supercell are simultaneously relaxed until the following conditions are met: (i) all the other five components (except σ_{zz}) of the Hellmann-Feynman stress tensor are negligibly small (<0.1 GPa), and (ii) the force on each atom becomes practically zero (<0.01 eV/Å). The shape of the (deformed) supercell, the positions of the atoms, and the relation between the tensile stress σ_{zz} and corresponding tensile strain ϵ_{zz} are determined completely at each step by this constrained atomic relaxation. The layers of the atoms, of which the z coordinates are fixed at each incremental deformation step [see Fig. 2(a)], are thick enough to prevent bond breaking near the artificial vacuum interfaces under tensile or compressive strains. The relation between tensile stress (σ_{zz}) and strain (ϵ_{zz}) are determined by [78]

$$\sigma_{zz} = \frac{1}{V}\frac{\partial E_{IF}}{\partial \epsilon_{zz}} \quad (1)$$

where E_{IF} and V are the total energy and volume of the interface supercell (including the inserted vacuum space), respectively, calculated in the VASP code. For real crystals, the calculated stress σ is independent of V, because if V increases, the number of atoms or E_{IF} inside V increases linearly. For supercell with vacuum space, however, its V changes if the vacuum space changes, but E_{IF} remains the same, so the calculated σ_{zz} becomes dependent on the vacuum space in V. The calculated stress should be rescaled by a factor c/c_0 to obtain the true stress, where c is the length of the supercell (including the vacuum space) in the z direction and c_0 is the effective atomic slab thickness inside the supercell. Here, we define c_0 as the distance between the bottom and top layers of pseudohydrogen. We tested the rescaled stress for supercells with a 25, 35, and 40 Å vacuum, and the results are nearly identical. This is similar to 2D heterojunction systems [79,80], where the stress obtained from the DFT calculation has to be rescaled to remove the vacuum space included in the supercell over which forces are being averaged.

C. Band alignment at heterojunction interfaces

The band alignment or offsets of a heterojunction is determined by the difference between the band gaps of two materials, which results in discontinued electron energy levels across the interface. This discontinuity or band alignment dictates mainly the carrier injection and transport properties of the heterojunction [51]. Generally, a natural VBO of semiconductors A and B is defined as [40,41]

$$VBO_{AB}^{(i)} = E_{\mathrm{v}}^{B} - E_{\mathrm{v}}^{A} + \Delta V_{P}^{(i)} + \Delta E_{D}^{(i)} \quad (2)$$

where B is the substrate and A is the material grown on top of the substrate, and i ($i = 1, 2, 3, 4$) stands for different interface bonding. The first two terms on the right-hand side express the bulk band edges of the two semiconductors determined by the difference between the valence band maximum (VBM) and macroscopic-averaged electrostatic potential (MAEP) of each bulk semiconductor. The third term ($\Delta V_{P}^{(i)}$) is the dipole potential resulted from the difference between the MAEP across the heterojunction calculated self-consistently [40,41], where dipole corrections to remove the artificial polar electric fields from the vacuum region are introduced [37]. Since the HSE hybrid functional requires huge computational resources and the difference between its results and those with GGA-PBE functional is within 50 meV [81], and our own electrostatic potential calculation tests for HSE and GGA-PBE using interface 1 as an example show nearly identical results (see Fig. S2 in SM for details [75]), so we obtain $\Delta V_{P}^{(i)}$ and all other quantities originated from the electrostatic potentials of the heterojunctions by GGA-PBE only. The dipole potential $\Delta V_{P}^{(i)}$ is determined by first the calculation of the electrostatic potential $V(x, y, z)$ of the heterojunction system, and its planar average over the plane parallel to the polar heterojunction interface, $\overline{V}(z)$, which varies only in the perpendicular z direction:

$$\overline{V}(z) = \frac{1}{S}\int_{S} V(x, y, z)dxdy \quad (3)$$

where S indicates the unit-cell area of the interface plane. This planar-averaged electrostatic potential oscillates quickly along the z axis because of the atomic spatial charge density variations of electrons and ionic cores, which can be averaged out over the fast oscillating atomic period l_0, giving rise to MAEP:

$$\widetilde{V}(z) = \frac{1}{l_0}\int_{z-l_0/2}^{z+l_0/2} \overline{V}(z')dz'. \quad (4)$$

Generally, MAEP is a flat constant for nonpolar planes, but there is an additional electric field induced by the polar heterojunction interfaces, which makes the MAEP inclined. By extrapolating the MAEP curves from each bulk-like region to the interface position, one can eliminate the effects of the polarization fields in determining the lineup of band gaps across the interface. Moreover, these polarization electric fields can generate additional confinement potentials for charge carriers in heterojunction supperlattices, as we discuss below.

The last term $\Delta E_{D}^{(i)}$ in VBO is the in-plane strain deformation potential. We calculate the deformation potential by constructing homogeneous junctions in a three-step method [50] (or see below for detailed calculation of $\Delta E_{D}^{(i)}$ for BAs/GaN heterojunctions). Finally, CBO of the heterojunction is obtained by the difference of the band gap E_g of each interface constituent,

$$CBO_{AB}^{(i)} = E_{g}^{B} - E_{g}^{A} + VBO_{AB}^{(i)} \quad (5)$$

where the same supercells of BAs/GaN heterojunction, plane wave cut-off energy, k grid and convergence criteria are used as those in ideal-stress calculation. We emphasize that HSE is adopted for the calculations of $E_{\mathrm{v}}^{A,B}$ and $E_{g}^{A,B}$, while all other results are obtained by GGA-PBE. The calculation method of the band offsets in the BAs/GaN superlattices is exactly the same as that for the heterojunctions.

III. RESULTS AND DISCUSSIONS

A. Interface energies and works of adhesion of BAs/GaN heterojunctions

The calculated lattice parameters of bulk BAs and GaN are listed in Table I, which agree well with the previous theoretical [44,83,85] and experimental results [24,84]. The stability of an interface at equilibrium can be evaluated by its interface energy (γ_{IF}), which is the excess energy per unit area after the interface is formed. A smaller γ_{IF} indicates an easier tendency to form the heterojunction interface. The interface energy of our heterojunction supercells is calculated by the following equation, which extends the definition of γ_{IF} by including the effect of hydrogen passivation [86–88], with the calculated results listed in Table I:

$$\gamma_{\mathrm{IF}} = \left(E_{\mathrm{IF}} - N_{\mathrm{BAs}}E_{\mathrm{BAs}}^{\mathrm{bulk}} - N_{\mathrm{GaN}}E_{\mathrm{GaN}}^{\mathrm{bulk}} - \sum \hat{E}_{\mathrm{H}}^{\mathrm{X}}\right)\Big/S - \sigma_{\mathrm{BAs}} - \sigma_{\mathrm{GaN}}, \quad (6)$$

$$\sigma_{\mathrm{BAs}} = \left(E_{\text{slab-BAs}} - nE_{\mathrm{BAs}} - m_{\mathrm{B}}\hat{E}_{\mathrm{H}}^{\mathrm{B}} - m_{\mathrm{As}}\hat{E}_{\mathrm{H}}^{\mathrm{As}}\right)/2A, \quad (7)$$

$$\sigma_{\mathrm{GaN}} = \left(E_{\text{slab-GaN}} - nE_{\mathrm{GaN}} - m_{\mathrm{Ga}}\hat{E}_{\mathrm{H}}^{\mathrm{Ga}} - m_{\mathrm{N}}\hat{E}_{\mathrm{H}}^{\mathrm{N}}\right)/2A, \quad (8)$$

where E_{IF} is the total energy of the BAs/GaN interface supercell; $E_{\mathrm{BAs}}^{\mathrm{bulk}}$ and $E_{\mathrm{GaN}}^{\mathrm{bulk}}$ are the total energies of a BAs and GaN bulk unit cell, respectively, with N_{BAs} and N_{GaN} the unit-cell numbers of BAs and GaN in the BAs/GaN interface supercell having an interface area S; $\hat{E}_{\mathrm{H}}^{\mathrm{X}}$ represents the energy of the pseudohydrogen attached to the X (X = B, As, Ga, or N) element, calculated based on a tetrahedral cluster [89–92]; $\sum \hat{E}_{\mathrm{H}}^{\mathrm{X}}$ indicates the summation of all the pseudo-hydrogen energies in the heterojunctions. σ_{BAs} and σ_{GaN} are surface energies of [111] BAs and [0001] GaN slabs with passivation pseudohydrogen atoms; $E_{\text{slab-M}}$ (M = BAs, GaN) is the total energy of the modeled slab with pseudohydrogen passivation; n is the number of the BAs (or GaN) bulk unit cells in the slab with a surface area A, while m_{X} is the number of pseudohydrogens attached to the X (X = B, As, Ga, or N) element in the slab.

The stability after formation of the polar BAs (111)/GaN (0001) heterojunction with interface 1-4 bonding types (see Fig. 2) are investigated by their work of adhesion (W_{ad}), which is the reversible work needed to separate an interface into two free surfaces, defined using the following formula [86,93]:

$$W_{ad} = \frac{E_{\mathrm{GaN}} + E_{\mathrm{BAs}} - E_{IF}}{S} \quad (9)$$

where E_{IF} is the total energy of the heterojunction as defined in Eq. (6), and E_{GaN} and E_{BAs} are the total energies of isolated GaN and BAs slabs, respectively, which are calculated by cutting the heterojunction supercells along the interface boundary into two separated slabs (see Fig. 2), so the effects of pseudohydrogen passivation cancel in W_{ad}. S represents the interface area. The obtained works of adhesion are also listed in Table I, where the positive values of W_{ad} indicate that the formed heterostructures are stable. To compare with the results of W_{ad}, we also calculated the energy barrier to pull a BAs/GaN heterojunction interface apart (see Fig. S3 in SM [75]) during tensile and compression deformations, which shows that the equilibrium heterojunction structures are all at the energy potential valley, indicating their stability. The increasing order of the energy barriers to pull the heterojunctions apart is consistent with that of W_{ad} for different heterojunction configurations.

We see from the Table I that the energy trends of γ_{IF} and W_{ad} are fairly consistent where a small γ_{IF} is correlated with a large W_{ad} (except for the interface 3), with the former governing the nucleation and growth of the heterojunction interface, and latter determining the mechanical strength of the heterojunction interface after formation under cleavage experiments. It is expected that interface 1 is easy to form with the smallest γ_{IF} and highest mechanical strength indicated by the largest W_{ad}, while interface 3 is also easy to form with the second smallest γ_{IF} and fairly high mechanical strength, and both of which can be synthesized since smooth N-polar and Ga-polar GaN substrates, which support interface 1 and 3, respectively, have been successfully obtained [94].

B. Ideal strengths of BAs/GaN heterojunctions

The ideal strength of crystals, which are the maximum stresses that crystals can sustain under various deformations, is one of the most fundamental mechanical properties of materials. For instance, the ideal tensile and compression strengths of a heterojunction normal to the interface determines its cleavage stability and resistance to compression stress when the heterojunction device is hit by an external impact or under large thermal-induced stresses, which is especially important for heterojunction devices working in hazardous environments. In order to understand the mechanical strength of the BAs/GaN heterojunction interfaces given in Fig. 2, we calculated the ideal tensile and compression strengths along their [0001] direction with the stress-strain curves plotted in Fig. 3, in comparison with those in bulk BAs along [111] and bulk GaN along [0001] directions, respectively. Under tensile strains, the maximum stresses for interface 1 and 2 reach 28.94 and 28.78 GPa, which are slightly lower than that (29.11 GPa) of bulk GaN in [0001] direction and about 2 GPa higher than that (26.71 GPa) of bulk BAs in [111] direction, while the tensile peak stresses for interface 3 (22.96 GPa) and 4 (22.15 GPa) are much lower. Beyond the maximum point, the stresses decrease rapidly with further increment of strain, and the heterojunctions are ultimately broken indicated by a decrease of stresses to nearly zero. As decohesion is important for understanding fracture or cleavage processes, bond length variations at selected tensile deformation stages are systematically analyzed, as shown in Fig. 4, with the corresponding bond lengths labeled in Fig. 2(b). The results in Fig. 4 show that for most of the interfaces (interface 2, 3, 4), the bonds (L_0) between two materials stretch and break first, while for interface 1, the strong B-N interface bond remains almost unchanged and the bonds (L_{-2}, L_{-3}) near the interface inside BAs lengthen and crack instead. For interfaces 3 and 4 where the As-Ga and As-N interface bonds are weak, they break at the critical strains of 9.5% and 9%, respectively, much earlier than the critical strains (13% and 14%) at the peak stress in bulk GaN [0001] and BAs [111] tensile direction, so the bond lengths away from the As-Ga and As-N interface vary little, as shown in Figs. 4(c) and 4(d). For interfaces 1 and 2 where the B-N and B-Ga interface bonds are strong, they crack at the critical strains of 13.5%, close to the critical strains in bulk GaN [0001] and BAs [111] tensile direction, so the bond lengths away from the B-N and B-Ga interface vary significantly, especially in the BAs part, which has a bulk tensile strength 2 GPa lower than that in bulk GaN, as shown in Figs. 4(a) and 4(b).

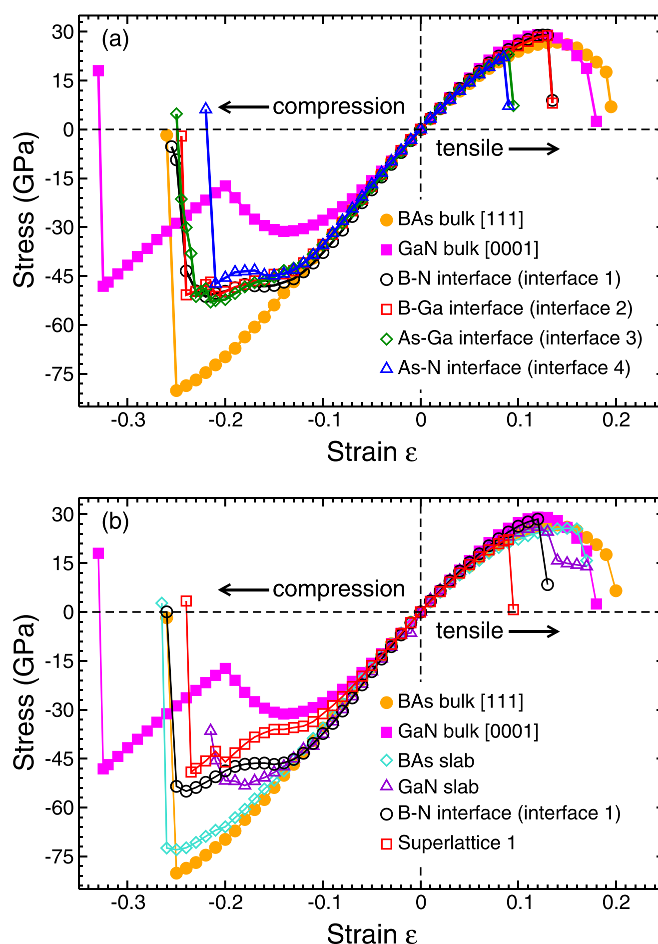

FIG. 3. (a) Tensile and compression stress–strain curves of BAs/GaN heterojunction for different interface configurations along [0001] direction normal to the interfaces. Also shown are the stress-strain curves for bulk GaN and BAs along [0001] and [111] directions, respectively. (b) Tensile and compression stress-strain curves of slab-GaN (8L), slab-BAs (9L) and SL-1 along [0001] direction. The other three curves are the same as those in (a), plotted for an easy comparison.

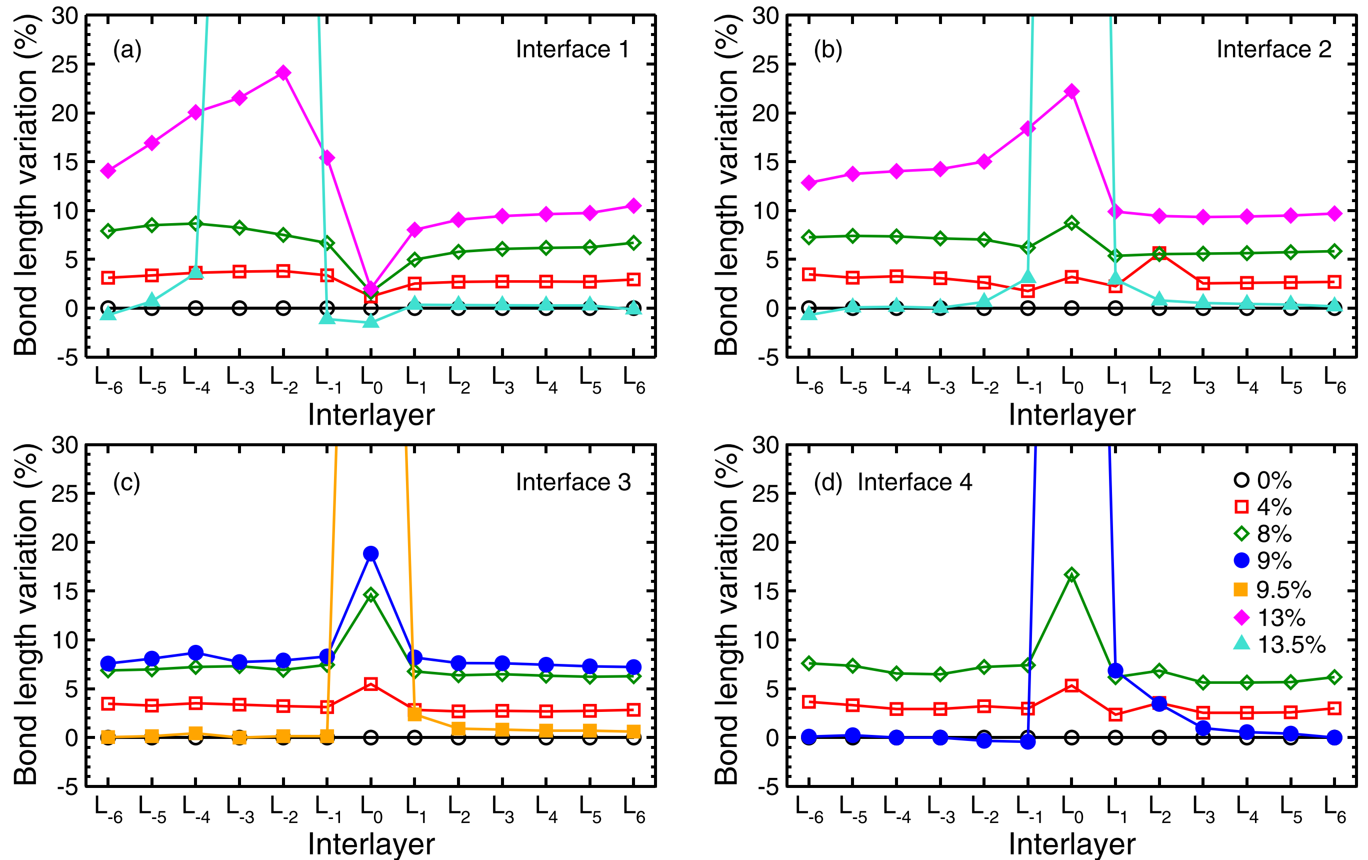

FIG. 4. [(a)–(d)] Variations of bond lengths in different atomic layers, as labeled in Fig. 2(b), at selected tensile strains for BAs/GaN heterojunctions with the interface 1-4 configurations.

For compression, the stress-strain curves of the four interfaces all lie between those of the two bulk materials, which differ considerably from each other, as shown in Fig. 3, indicating a large enhancement of strength or stiffness of the BAs/GaN heterojunction interfaces, especially for compression strains in the range 0 ∼ –20%. The highest compression stresses, that is the compression strengths, of the interface 1-4 are about 50 GPa, much higher than that (31.8 GPa) of bulk GaN. To understand the mechanism of this enhanced stiffness, we plot in Fig. 5 the snapshots of bulk GaN and BAs/GaN heterojunction with interface 1 compressed in [0001] direction. For bulk GaN, its *ABAB*... stacking structure in [0001] direction allows the formation of new Ga-N bonds between neighboring (0001) layers under large compression (–20%), which will partially compensate the energy increase during compression, accompanied by a structural transformation from symmetry P63mc (No.186) to P63/mmc (No.194), as shown in Figs. 5(a)–5(c). During the structural transformation, the Ga-N bond length between neighboring (0001) layers, designated as R in Fig. 5, decreases first under compression until the compression stress reaches its maximum, and then R increases causing a reduction of the compression stress, as shown by the solid cubic curve in Fig. 3. Such a structural transformation does not exist in bulk BAs under [111] compression, since its $A'B'C'A'B'C'$... stacking does not allow the formation of new B-As bonds between neighboring (111) layers [see Fig. 5(d)]. The energy of bulk BAs increases continuously under [111] compression, which results in a much higher compression strength compared to that in bulk GaN. For the BAs/GaN heterojunction interfaces under [0001] compression, the same structural transformation in its GaN part still happens, but the increase of the Ga-N bond length (R) between neighboring (0001) layers disappears due to the strong compression strength in the BAs part, as shown in Figs. 5(d)–5(f), which enhances the strength or stiffness of the heterojunctions. Under compression, the instability of the heterojunctions is signaled by sudden large bond angle variations. So we plot bond angles (α_i) in different atomic layers, as labeled in Fig. 2(c), at selected compression strains in Fig. 6 before the structural collapses set in. During the compression process, the deformation of bond angles (α_i) inside GaN is generally larger than that (α_{-i}) inside BAs, indicating a lower stiffness in GaN. And the collapse of the heterojunctions under compression are always triggered by the sudden increase in α_1 close to the interfaces, when the compression strains approach to about –21%.

We also calculate the stress-strain curves of slab-GaN, slab-BAs, and BAs/GaN superlattice structures, in comparison with those of the heterojunction interface 1, bulk BAs and GaN, as shown in Fig. 3(b). To apply compression (or tension) on a slab using the supercell model with inserted vacuum space, one has to fix the relaxation of atoms on the surfaces of the slab during each step of the incrementally compressive deformations, as we did for the compression of the heterojunction interface supercells [see Fig. 2(a)]. Our results reveal that both BAs/GaN interfaces and fixed GaN

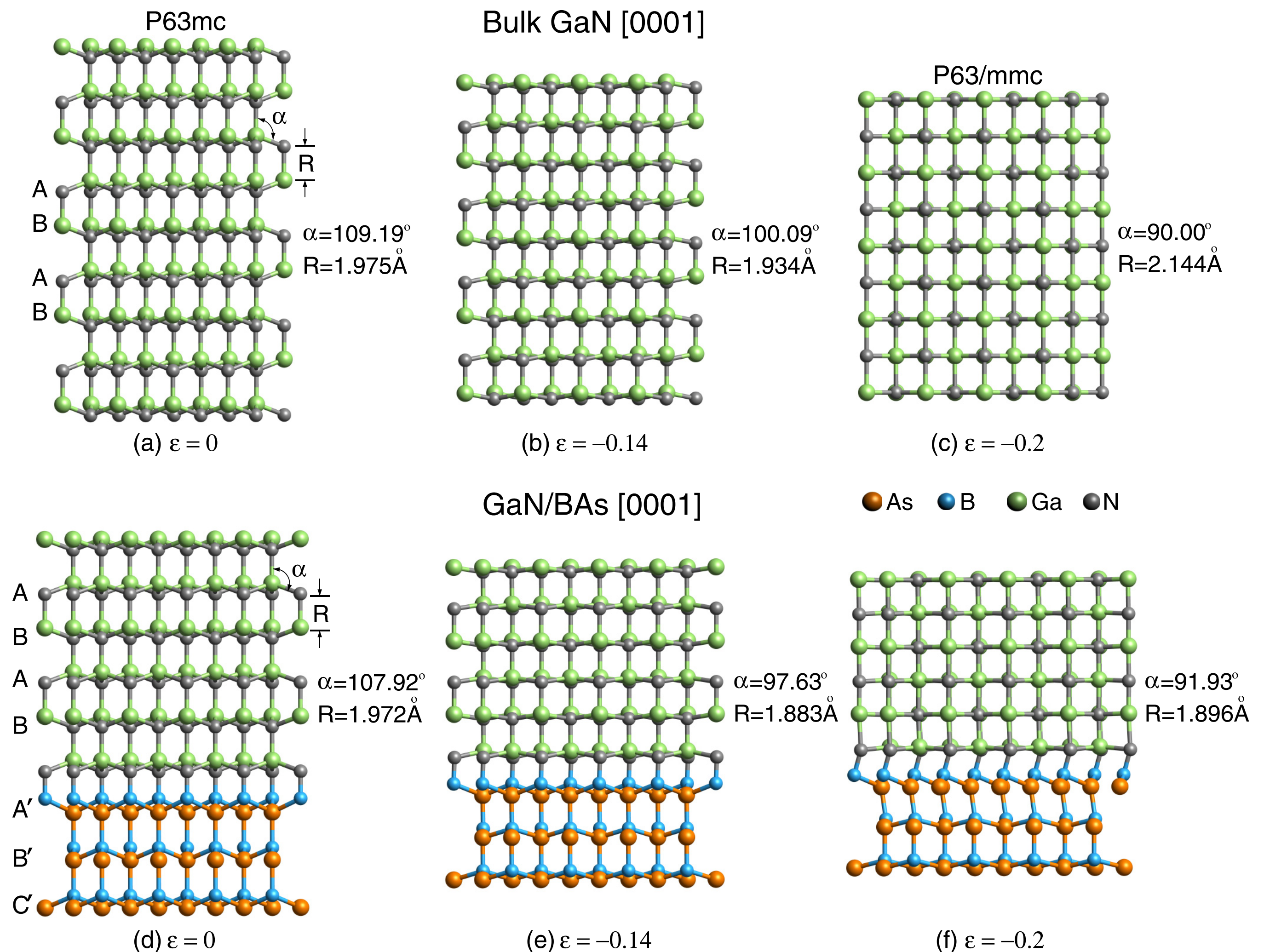

FIG. 5. [(a)–(c)] Snapshots of bulk GaN compressed in [0001] direction at (a) $\epsilon = 0$ (equilibrium structure), (b) $\epsilon = -0.14$ (peak stress) and (c) $\epsilon = -0.2$ (structural phase transformation from P63mc (No.186) to P63/mmc (No.194)). [(d)–(f)] Snapshots of BAs/GaN heterojunction with a B-N interface compressed in [0001] direction at the same compression strains as those in (a)–(c).

surfaces can enhance the compression strength of bulk GaN, where the GaN slab has two fixed surfaces, the supercell of heterojunction interface 1 has one BAs/GaN interface and one fixed GaN surface, and the BAs-GaN superlattice has only BAs/GaN interfaces. All their compression strengths are enhanced compared to that of bulk GaN. The mechanisms are the same, where both the BAs/GaN interfaces and fixed GaN surfaces prevent the increase of the Ga-N bond length (R) between neighboring (0001) layers in GaN under compression induced structural transformation from symmetry P63mc to P63/mmc [see Figs. 5(a)–5(c)]. In addition, the elastic constants and Poisson's ratios describe the material strength near its equilibrium structure. So we calculate the elastic constants and Poisson's ratios of the heterojunction interface 1-4, in comparison with those of bulk BAs and GaN. The corresponding results are given in Table S2 in SM [75].

C. Polar band offsets of BAs/GaN heterojunctions

Band offsets at heterostructure interfaces are essential to characterize the function and performance of semiconductor heterostructure devices, such as transistors, solid lasers, light-emitting devices and so on. In this section, we first considered (0001) polar plane of GaN as substrate with fixed lattice parameters, while (111) polar plane of BAs is grown on its top with the same in-plane lattice constants [26], where the heterojunction supercell is separated by a 40 Å vacuum space, as shown in Fig. 2. Moreover, one bottom bilayer of GaN atoms together with its passivation pseudohydrogen atoms are fixed, whereas the other atoms are allowed to relax freely, in order to facilitate the simulation of a GaN substrate. Therefore, a 5.5% (calculated) lattice mismatch exists in BAs/GaN heterostructure interfaces formed between BAs (111) and GaN (0001) planes, which means the necessity of including the deformation potentials $\Delta E_D^{(i)}$ to estimate the band alignments. To obtain $\Delta E_D^{(i)}$ in BAs (111) plane, a homojunction model is adopted following a three-step method [50]. It should be noted that if the lattice parameters of GaN are fixed, $\Delta E_D^{(i)}$ comes only from the deformation of BAs (111) plane. Otherwise, both deformed BAs (111) and GaN (0001) planes make contributions to $\Delta E_D^{(i)}$, as we show later for BAs/GaN superlattices. In order to calculate the deformation potential

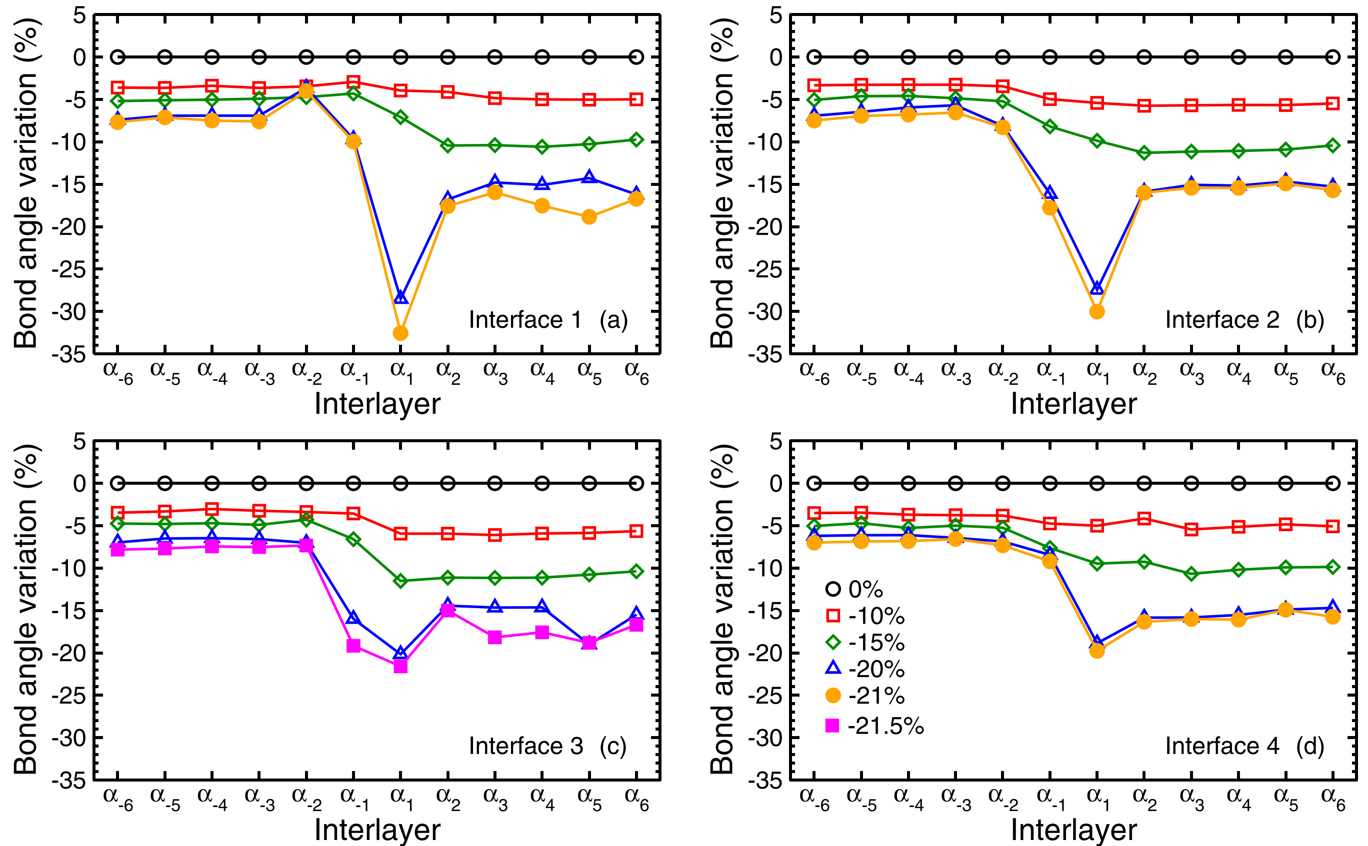

FIG. 6. [(a)–(d)] Variations of bond angles in different atomic layers, as labeled in Fig. 2(c), at selected compression strains for BAs/GaN heterojunctions with the interface 1-4 configurations before the heterojunctions collapse.

in BAs (111) plane, we create a new orthorhombic supercell (a_1, a_2, a_3) for BAs with its a_3 parallel to its original [111] direction, as plotted in Fig. 7(a), and allow the lattice parameters of BAs to change to (b_1, b_2, a_3) following the two steps described in Figs. 7(c) and 7(d), where (b_1, b_2, b_3) are lattice parameters of a orthorhombic supercell (b_1, b_2, b_3) for GaN with its b_3 parallel to its original [0001] direction, as plotted in Fig. 7(b). Then, the total $\Delta E_D^{(i)}$ is calculated as $\widetilde{V}_{b_1,b_2,a_3} - \widetilde{V}_{a_1,a_2,a_3}$, with MAEP $\widetilde{V}$ defined in Eq. (3) and Eq. (4). Since the in-plane lattice constant of the heterojunction is fixed to that of GaN, the deformation potentials of the four interface bonding are the same. We also calculate the electrostatic potential of the above BAs homojunction model in the presence of pseudohydrogen (see Fig. S4 in SM [75]), which are nearly identical to those calculated without pseudohydrogen. This is because the deformation potential is calculated on a nonpolar plane, so the presence of pseudohydrogen does not affect the result. According to the calculated results given in Table II, the deformation potential of BAs (111) plane along a_1 and a_2 axis is 0.73 eV and 0.72 eV, respectively. The large values show that $\Delta E_D^{(i)}$ must be taken into account in order to obtain natural band offsets correctly.

It is well known that wurtzite semiconductors (e.g., GaN) exhibit a nonvanish dipole in [0001] direction, in which the centers of positive and negative charges do not coincide due to the lack of inversion symmetry. Moreover, the (111) surface of zinc-blend structures (e.g., BAs) will produce piezoelectric polarization due to the effect of strain. These polarization fields induce internal electric fields and cause MAEP inclined inside materials. The planar averaged electrostatic potentials, $\overline{V}(z)$ in Eq. (3), and MAEP, $\widetilde{V}(z)$ in Eq. (4), of the four BAs/GaN heterojunction interfaces are shown in Fig. 8. Apart from a few atomic layers close to the heterojunction and vacuum interfaces, MAEP (red curves) inside two materials can be well fitted with declined straight lines (green lines) using the method of linear least squares. The difference in MAEP at the heterojunction interface, which is defined as the polar dipole potential $\Delta V_P^{(i)}$, is given in Table III. In order to test the calculation accuracy, we gradually increase the number of atomic layers in the BN interface model [see Fig. 2(a)] from 9BAs/8GaN to 21BAs/30GaN layers, which shows a variation of $\Delta V_P^{(i)}$ less than 4%, indicating sufficient numbers of atomic layers we adopted. The large $\Delta V_P^{(i)}$ appears at the interfaces near which strong built-in polarization electric fields (steep MAEP slopes) exist inside the heterojunctions.

With the calculated deformation and polar dipole potentials, the in-plane strained (without $\Delta E_D^{(i)}$) and natural (with $\Delta E_D^{(i)}$) band offsets of the BAs/GaN heterojunctions for different interface configurations are presented in Table III. We can clearly see that the values and types of the band offsets not only depend critically on the interfacial atomic structures (configurations), but also sensitively on the deformation potential energy. The band offset line-ups with and without $\Delta E_D^{(i)}$ for the four BAs/GaN heterojunction interfaces are

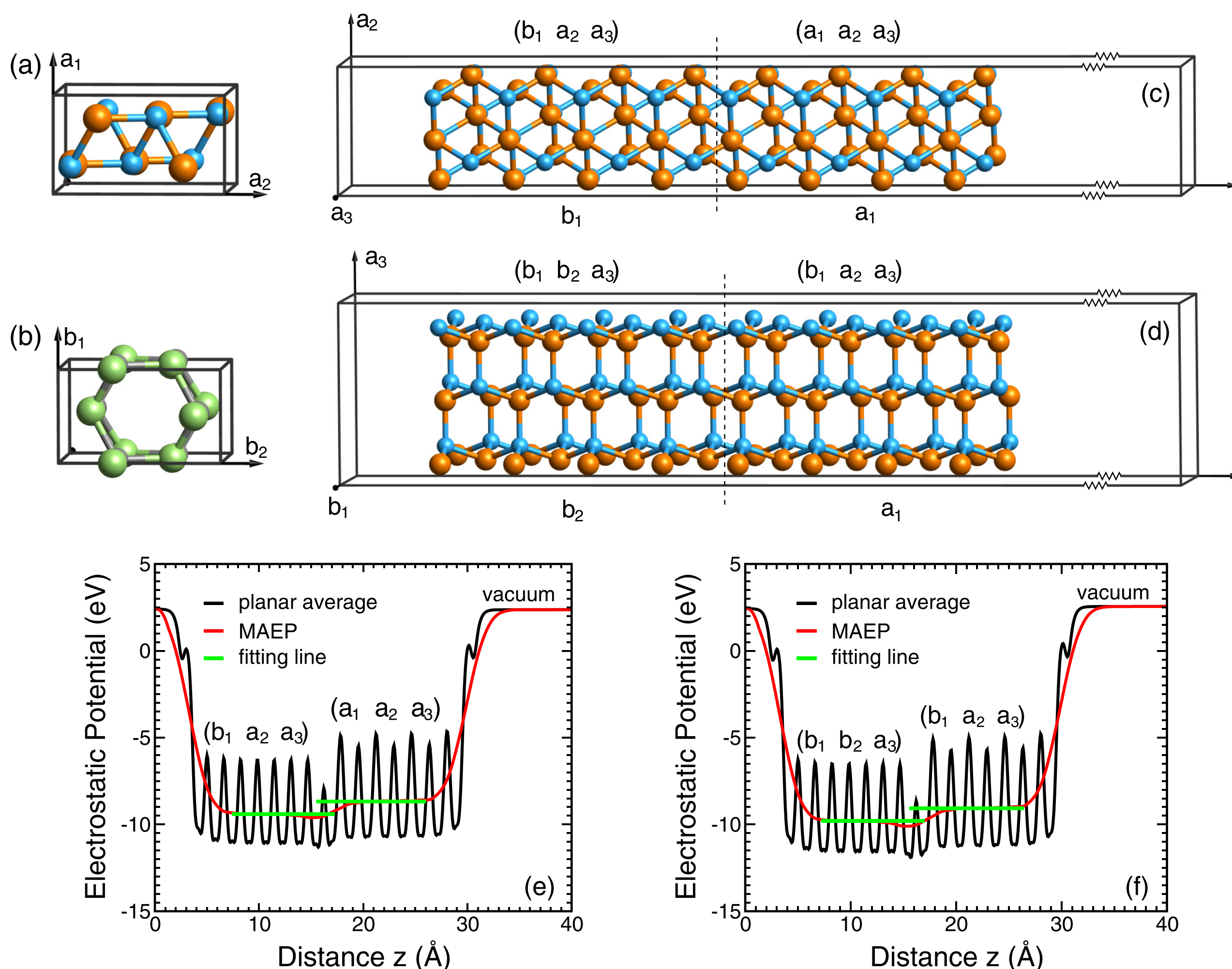

FIG. 7. [(a),(b)] The orthorhombic supercells of BAs and GaN bulk crystals. [(c),(d)] The homojunction structure of BAs used to calculate the deformation potential in a_1 and a_2 directions by the three-step method, with the calculated averaged electrostatic potentials given in (e) and (f), respectively.

depicted in Fig. 9. Most of the heterojunction interfaces, such as 1, 3, and 4, show a type-II natural band alignments, which can effectively prevent carrier recombination and improve photocatalytic efficiency for semiconductor photocatalysis applications [95]. This is different from the previous study on $In_xGa_{1-x}N$/BAs heterostructure proposed for photovoltaic device applications, where the calculation revealed a type-II band alignment with $0.3 < x < 1$, while a type-I band alignment was predicted for GaN/BAs ($x = 0$) [26]. Even for the interface 2, which exhibits a type-I band offset, one can notice a large MAEP up-bending near the interface [see Fig. 8(b)], which gives rise to a polarization induced electric field that expels electrons from and attracts holes towards the interface. Such polarization induced electric fields have been proposed to generate saw-tooth-like potentials in zincblende-wurtzite superlattices for efficient electron-hole separation with application in hydrogen production by solar water splitting [42]. Moreover, our results shown below that in forming BAs/GaN superlattices, all the four interfaces become type-II band alignment, suitable for semiconductor photocatalysis

TABLE II. Lattice parameters of the orthorhombic supercell, lattice mismatches, HSE band gaps (E_g), VBM positions (E_v) relative to the MAEP of bulk BAs and GaN, together with the deformation potential energy ($\Delta E_D^{(i)}$) in each direction and total summation due to the lattice mismatch in BAs. $\Delta E_D^{(i)}$ is the same in all the heterojunction interfaces when the lattice parameters of GaN are fixed.

	Lattice parameter (Å)		Lattice mismatch (%)				$\Delta E_D^{(i)}$ in each direction (eV)		
Compounds	a_1	a_2	a_1	a_2	E_g (eV)	E_v (eV)	a_1	a_2	Total $\Delta E_D^{(i)}$ (eV)
BAs	3.406	5.899	–5.50	–5.50	1.90	5.25	–0.73	–0.72	–1.45
GaN	3.219	5.575	0.00	0.00	3.51	3.84	0.00	0.00	

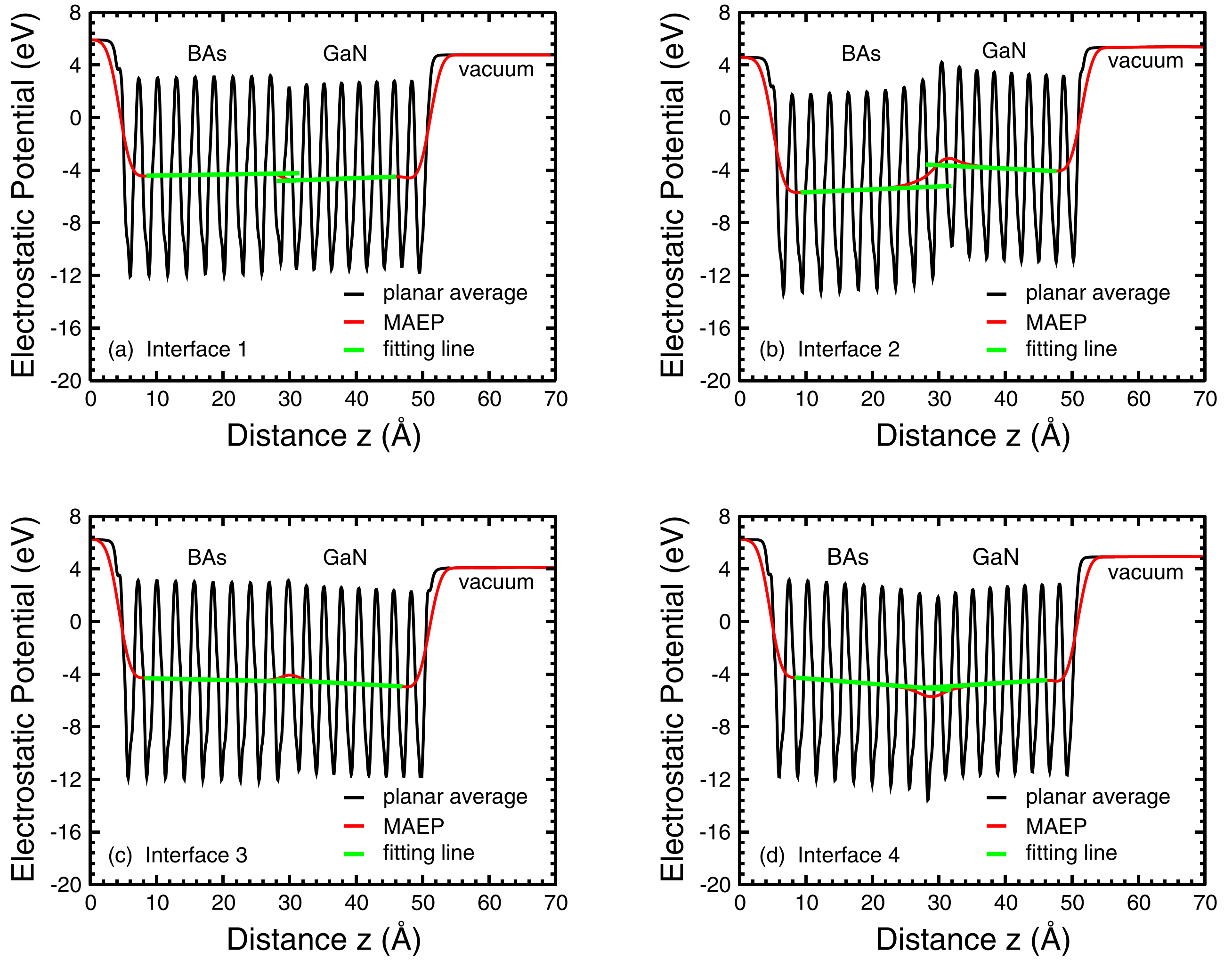

FIG. 8. [(a)–(d)] Planar average $\overline{V}(z)$ and macroscopic average (MAEP) $\widetilde{V}(z)$ of electrostatic potentials of BAs/GaN heterojunctions for interface 1-4 configurations.

applications. We also calculate the density of states on each layer (LDOS) of the heterojunction interfaces (see Fig. S5 and Table S3 in SM [75]), which show that interface states inside the band gaps appear on a few atomic layers closest to the heterojunction interfaces.

D. Polar band offsets of BAs/GaN superlattices

In practical applications, semiconductor heterojunctions are exploited to design various unique structures, such as superlattices or multiple quantum wells (MQWs), in order to increase active regions, enhance luminescence efficiencies, and adjust electronic bands for applications in photovoltaics [96,97], photocatalytics [42], photostrictive materials [98], light-emitting-diodes [99], and long-wave length infrared detection [100] etc. Here, we further study (111) BAs/(0001) GaN superlattice structures, which due to the crystalline symmetries of BAs (zincblende) and GaN (wurtzite) either contains the B-N and As-Ga interfaces (designated as SL-1), or As-N and B-Ga interfaces (SL-2), as shown in Fig. 10. The optimized in-plane lattice constants (a_1, a_2) or (b_1, b_2) [see Figs. 7(a) and 7(c)] for SL-1 and SL-2 are (3.315, 5.742) and

TABLE III. Dipole potential energy ($\Delta V_P^{(i)}$), valence ($VBO^{(i)}$) and conduction ($CBO^{(i)}$) band offset with and without deformation potential energy ($\Delta E_D^{(i)}$) of BAs/GaN heterojunctions for different interface configurations (in units of eV), together with the type of the heterojunctions.

Interface bonding	$\Delta V_P^{(i)}$	$VBO^{(i)}$		$CBO^{(i)}$		Type	
		Without $\Delta E_D^{(i)}$	With $\Delta E_D^{(i)}$	Without $\Delta E_D^{(i)}$	With $\Delta E_D^{(i)}$	Without $\Delta E_D^{(i)}$	With $\Delta E_D^{(i)}$
1 (B-N bonding)	–0.52	–1.93	–3.38	–0.32	–1.77	II	II
2 (B-Ga bonding)	1.52	0.11	–1.34	1.72	0.27	II	I
3 (As-Ga bonding)	0.15	–1.26	–2.71	0.35	–1.10	I	II
4 (As-N bonding)	0.26	–1.15	–2.60	0.46	–0.99	I	II

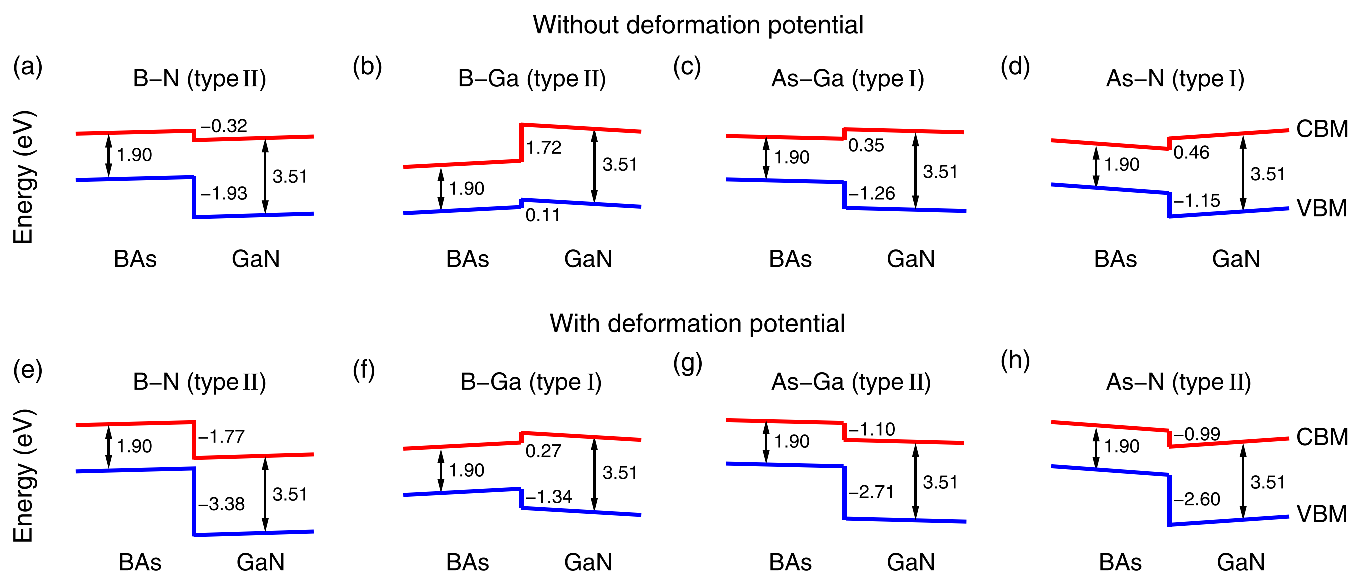

FIG. 9. [(a)–(d)] The band alignments without the deformation potential energies and [(e)–(h)] the band alignments with deformation potential energies for different BAs/GaN heterojunction interface 1-4 configurations.

(3.314, 5.740) Å, which result in a nearly identical lattice mismatch of –2.5% and 3.0% in BAs and GaN, respectively. The obtained total deformation potential $\Delta E_D^{(i)}$ is 1.36 eV for both superlattices. An important character of the superlattice is the band offsets at the interfaces. Figures 11(a) and 11(b) show the planar average electrostatic potential and MAEP of SL-1 and SL-2, from which the polar dipole potential $\Delta V_P^{(i)}$ and the (natural) band offsets are determined, given in Table IV. The periodical band alignments of the superlattices are shown in Figs. 11(c) and 11(d), which reveal that all the four interfaces are type II, with the band offsets marginally different from those in the heterojunctions because the relaxed equilibrium structures of the superlattices differ slightly from those of the heterojunctions. A large alternately directed built-in electric field is found in SL-2, coming from the sawtooth-like polar dipole potential, which can effectively separate electrons and holes to different interfaces, desirable for the photocatalytic processes. Comparing the slopes of the MAEP curves in Fig. 8 and Figs. 11(a) and 11(b), we can see that the built-in electric fields in SL-2 are about 3 ∼ 5 times stronger than those in the corresponding heterojunctions, demonstrating an effective way to enhance and adjust the polarization electric fields in SL-2 due to its repeated positively and negatively charged N-As and Ga-B interfaces. For SL-1, however, the built-in electric fields have only a small increment compared to those in the heterojunctions. Figures 11(d) and 11(f) suggest that the Ga-B interfaces repel, while the As-N interfaces attract electrons. Since Ga and B are III-group elements, they require extra electrons to form sp^3 bonding of the Ga-B interface. Therefore, the total charge on the Ga-B interface is negative, which repels other electrons (that is, the electric field E points to the Ga-B interface). Analogously, as As and N are V-group elements, they only contribute four electrons to form sp^3 bonding of the As-N interface, and other electrons can

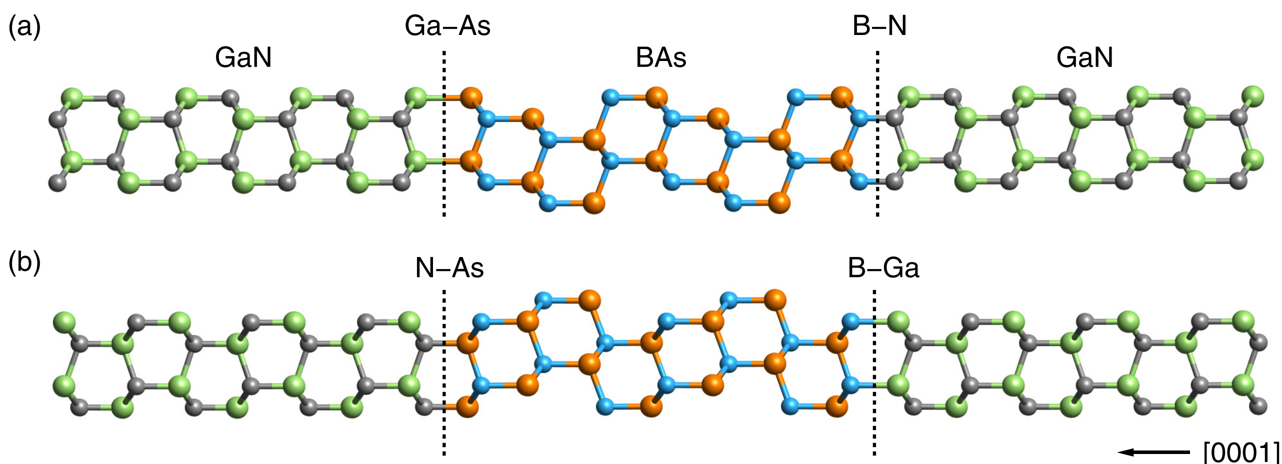

FIG. 10. (a) The superlattice structure of SL-1 with B-N and As-Ga interfaces. (b) The superlattice structure of SL-2 with B-Ga and As-N interfaces.

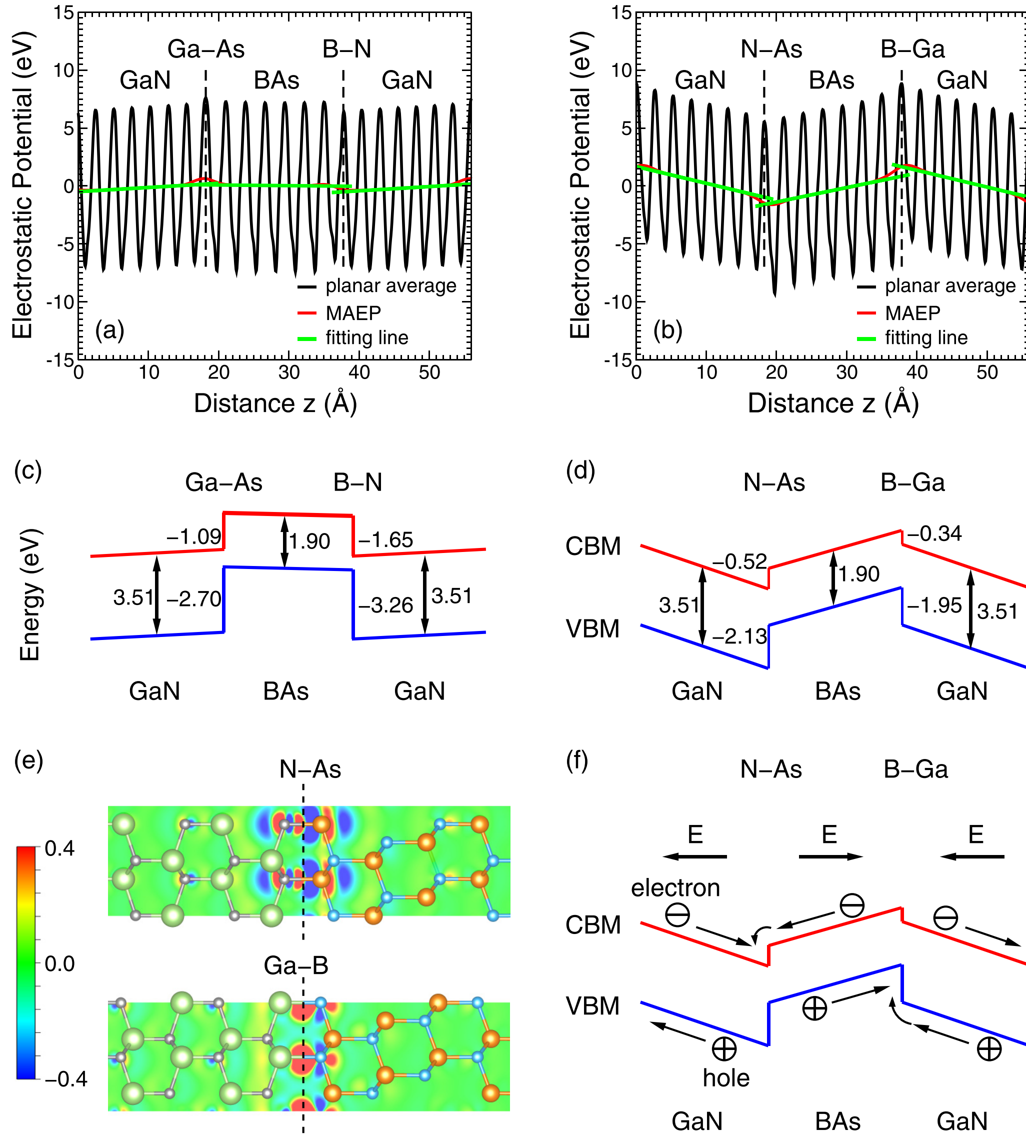

FIG. 11. [(a),(b)] Planar average $\overline{V}(z)$ and macroscopic average (MAEP) $\widetilde{V}(z)$ of electrostatic potential of the SL-1 and SL-2 superlattices. [(c),(d)] The band alignment diagrams of SL-1 and SL-2. (e) Electron density difference Δn (in unit of $10^{-2}/a_B^3$ with a_B the Bohr radius) for SL-2 with B-Ga and As-N interface on a $(\bar{1}2\bar{1}0)$ crystallographic plane. (f) The illustration of electron–hole separations in SL-2.

TABLE IV. Dipole potential energy ($\Delta V_P^{(i)}$), valence ($VBO^{(i)}$), and conduction ($CBO^{(i)}$) band offset including the deformation potential energy ($\Delta E_D^{(i)}$) (in units of eV), together with the type of the heterojunctions, for different interface configurations in BAs/GaN superlattice SL-1 and SL-2.

Interface bonding	$\Delta V_P^{(i)}$	$VBO^{(i)}$	$CBO^{(i)}$	Type	Super -lattice
1 (B-N bonding)	−0.49	−3.26	−1.65	II	SL-1
2 (B-Ga bonding)	0.82	−1.95	−0.34	II	SL-2
3 (As-Ga bonding)	0.07	−2.70	−1.09	II	SL-1
4 (As-N bonding)	0.64	−2.13	−0.52	II	SL-2

leave the interface, so the total charge at the As-N interface is positive, which attracts other electrons. The explanation is consistent with the calculated electron density difference on a $(\bar{1}2\bar{1}0)$ crystallographic plane for SL-2, as plotted in Fig. 11(e), where the regions with decreased electron density are in blue, and those with increased ones are in red. This also explains why SL-1 with the B-N and Ga-As interfaces only has a weak polar dipole potential since its interfaces consist of III- and V-group elements, which form perfect sp^3 bonds on the interface and show weak total charge variations. Figure 11(f) demonstrates electron and hole separation in SL-2. Once electron-hole pairs are created anywhere in SL-2 by incident lights, electrons and holes move to different interfaces. Our study shows that both SL-1 and SL-2 BAs/GaN superlattices can be applied to photocatalytic devices, and the

internal polarization electric field of SL-2 can further enhance the efficiency of the catalysis processes.

IV. CONCLUSIONS

The ideal tensile and compressive strengths and band alignments for BAs (111)/GaN (0001) heterojunctions and superlattices with four interface configurations were investigated in this paper. The results show that the B-N and B-Ga interface configurations are the two most stable heterojunctions with their normal tensile strengths nearly as strong as those in bulk BAs [111] and GaN [0001] directions, while the As-Ga and As-N interfaces are much weaker and break up earlier under normal tensile stresses. Under normal compression, all the four BAs/GaN heterojunction interfaces show much higher compressive stiffness compared to that in bulk GaN [0001] direction, where the zincblende BAs suppresses the softening of wurtzite GaN during a structural transformation from symmetry P63mc to P63/mmc under compressive stresses. The high compressive stiffness of the BAs/GaN heterojunction can protect its electronic properties from drastic changes under external impacts. The natural band alignments of the mismatched BAs/GaN heterojunctions are calculated by a three-step approach, which indicates that most of the heterojunction interfaces give rise to type-II staggered systems, while only B-Ga interface results in a type-I straddling band alignment. Moreover, in BAs/GaN superlattices, all the natural band alignments of heterojunction interfaces are type-II. Especially in the superlattice with repeatedly positive- and negative-charged N-As and Ga-B interfaces, a large polarization built-in electric field exists, inducing a sawtooth-like polar dipole potential, which can effectively separate electrons and holes to different interfaces, desirable for the photocatalytic processes. Our calculations show that BAs/GaN heterojunctions can not only provide a much-needed alternative to GaN-on-SiC or GaN-on-diamond heat dissipation systems in future designing of high-power electronic and optoelectronic devices, but also offer new possibilities of applications in photovoltaic, photodiode, and photocatalytic devices as a type-II semiconductor heterojunction or superlattice.

ACKNOWLEDGMENTS

This work was supported by the National Natural Science Foundation of China (Grant No. 11974237). Computations were performed at the Center for High Performance Computing, Shanghai Jiao Tong University.

[1] H. Amano, Y. Baines, E. Beam, M. Borga, T. Bouchet, P. R. Chalker, M. Charles, K. J. Chen, N. Chowdhury, R. Chu *et al.*, The 2018 GaN power electronics roadmap, J. Phys. D: Appl. Phys. **51**, 163001 (2018).

[2] T. J. Flack, B. N. Pushpakaran, and S. B. Bayne, GaN technology for power electronic applications: A review, J. Electron. Mater. **45**, 2673 (2016).

[3] N. Ikeda, Y. Niiyama, H. Kambayashi, Y. Sato, T. Nomura, S. Kato, and S. Yoshida, GaN power transistors on Si substrates for switching applications, Proc. IEEE **98**, 1151 (2010).

[4] Y.-f. Wu, M. Moore, A. Saxler, T. Wisleder, and P. Parikh, 40-W/mm double field-plated GaN HEMTs, in *2006 64th Device Research Conference* (IEEE, State College, PA, USA, 2006) pp. 151–152

[5] T. Ohki, A. Yamada, Y. Minoura, K. Makiyama, J. Kotani, S. Ozaki, M. Sato, N. Okamoto, K. Joshin, and N. Nakamura, An over 20-W/mm s-band InAlGaN/GaN HEMT with SiC/Diamond-bonded heat spreader, IEEE Electron Device Lett. **40**, 287 (2019).

[6] A. J. Suria, A. S. Yalamarthy, T. A. Heuser, A. Bruefach, C. A. Chapin, H. So, and D. G. Senesky, Thickness engineering of atomic layer deposited Al_2O_3 films to suppress interfacial reaction and diffusion of Ni/Au gate metal in AlGaN/GaN HEMTs up to 600 °C in air, Appl. Phys. Lett. **110**, 253505 (2017).

[7] D. Maier, M. Alomari, N. Grandjean, J.-F. Carlin, M.-A. Diforte-Poisson, C. Dua, S. Delage, and E. Kohn, InAlN/GaN HEMTs for operation in the 1000 °C regime: A first experiment, IEEE Electron Device Lett. **33**, 985 (2012).

[8] D. T. Morelli, J. P. Heremans, C. P. Beetz, W. S. Yoo, and H. Matsunami, Phonon-electron scattering in single crystal silicon carbide, Appl. Phys. Lett. **63**, 3143 (1993).

[9] R. Wei, S. Sheng, K. Yang, Y. Cui, P. Yan, X. Chen, X. Hu, and X. Xu, Thermal conductivity of 4H-SiC single crystals, J. Appl. Phys. **113**, 283 (2013).

[10] Y. Bai, Z. Jin, X. Lv, Z. Jiang, X. Han, J. Wang, and H. Wu, High rate growth of thick diamond films by high-current hot-cathode PCVD, J. Cryst. Growth **280**, 539 (2005).

[11] M. Aslam, G. Yang, and A. Masood, Boron-doped vapor-deposited diamond temperature microsensors, Sens. Actuators, A **45**, 131 (1994).

[12] A. El-Helou, Y. Cui, M. J. Tadjer, T. J. Anderson, D. Francis, T. Feygelson, B. Pate, K. D. Hobart, and P. E. Raad, Full thermal characterization of AlGaN/GaN high electron mobility transistors on silicon, silicon carbide, and diamond substrates using a reverse modeling approach, Semicond. Sci. Technol. **36**, 014008 (2021).

[13] Z. Li and R. C. Bradt, Thermal expansion of the hexagonal (4H) polytype of SiC, J. Appl. Phys. **60**, 612 (1986).

[14] M. Stockmeier, R. Müller, S. A. Sakwe, P. J. Wellmann, and A. Magerl, On the lattice parameters of silicon carbide, J. Appl. Phys. **105**, 033511 (2009).

[15] S. Li, K. M. Taddei, X. Wang, H. Wu, J. Neuefeind, D. Zackaria, X. Liu, C. D. Cruz, and B. Lv, Thermal expansion coefficients of high thermal conducting BAs and BP materials, Appl. Phys. Lett. **115**, 011901 (2019).

[16] X. Chen, C. Li, F. Tian, G. A. Gamage, S. Sullivan, J. Zhou, D. Broido, Z. Ren, and L. Shi, Thermal Expansion Coefficient and Lattice Anharmonicity of Cubic Boron Arsenide, Phys. Rev. Appl. **11**, 064070 (2019).

[17] B. Srikanta and S. K. Mazumder, Fabrication and characterization of a GaN/(4H)SiC vertical pn power diode using direct and interfaced epitaxial-growth approaches, J. Semicond. **34**, 044001 (2013).

[18] E. Kojima, K. Endo, H. Shirakawa, K. Chokawa, M. Araidai, Y. Ebihara, T. Kanemura, S. Onda, and K. Shiraishi, First principles investigation of SiC/AlGaN(0001) band offset, J. Cryst. Growth **468**, 758 (2017).

[19] S. Madhusoodhanan, S. Sandoval, Y. Zhao, M. E. Ware, and Z., A highly linear temperature sensor using GaN-on-SiC heterojunction diode for high power applications, IEEE Electron Device Lett. **38**, 1105 (2017).

[20] M. Tyhach, D. Altman, S. Bernstein, R. Korenstein, J. Cho, K. E. Goodson, D. Francis, F. Faili, F. Ejeckam, S. Kim, and S. Graham, S2-T3: Next generation gallium nitride HEMTs enabled by diamond substrates, in *2014 Lester Eastman Conference on High Performance Devices (LEC)* (IEEE, Ithaca, NY, USA, 2014) pp. 1–4.

[21] Y. Won, J. Cho, D. Agonafer, M. Asheghi, and K. E. Goodson, Fundamental cooling limits for high power density gallium nitride electronics, IEEE Trans. Compon. Packag. Manuf. **5**, 737 (2017).

[22] J. S. Kang, M. Li, H. Wu, H. Nguyen, T. Aoki, and Y. Hu, Integration of boron arsenide cooling substrates into gallium nitride devices, Nat. Electron. **4**, 416 (2021).

[23] F. Tian, B. Song, X. Chen, N. K. Ravichandran, Y. Lv, K. Chen, S. Sullivan, J. Kim, Y. Zhou, and T. H. Liu, Unusual high thermal conductivity in boron arsenide bulk crystals, Science **361**, 582 (2018).

[24] J. S. Kang, M. Li, H. Wu, H. Nguyen, and Y. Hu, Experimental observation of high thermal conductivity in boron arsenide, Science **361**, 575 (2018).

[25] S. Li, Q. Zheng, Y. Lv, X. Liu, X. Wang, P. Y. Huang, D. G. Cahill, and B. Lv, High thermal conductivity in cubic boron arsenide crystals, Science **361**, 579 (2018).

[26] K. Bushick, S. Chae, Z. Deng, J. T. Heron, and E. Kioupakis, Boron arsenide heterostructures: Lattice-matched heterointerfaces and strain effects on band alignments and mobility, npj Comput. Mater. **6**, 3 (2020).

[27] J. E. Herriman, O. Hellman, and B. Fultz, Phonon thermodynamics and elastic behavior of GaN at high temperatures and pressures, Phys. Rev. B **98**, 214105 (2018).

[28] S. Lyu and W. R. L. Lambrecht, First-principles study of the phonon replicas in the photoluminescence spectrum of 4H-SiC, Phys. Rev. B **101**, 045203 (2020).

[29] M. Fan, W. Cen, X. Cai, Y. Liao, J. Xie, and Q. Xie, The defects regulating for the electronic structure and optical properties of 4H-SiC with (0001) surface, Appl. Surf. Sci. **427**, 851 (2018).

[30] X. Meng, A. Singh, R. Juneja, Y. Zhang, F. Tian, Z. Ren, A. K. Singh, L. Shi, J.-F. Lin, and Y. Wang, Pressure-dependent behavior of defect-modulated band structure in boron arsenide, Adv. Mater. **32**, 2001942 (2020).

[31] I. Bravić and B. Monserrat, Finite temperature optoelectronic properties of BAs from first principles, Phys. Rev. Mater. **3**, 065402 (2019).

[32] T. H. Liu, B. Song, L. Meroueh, Z. Ding, Q. Song, J. Zhou, M. Li, and G. Chen, Simultaneously high electron and hole mobilities in cubic boron-V compounds: BP, BAs and BSb, Phys. Rev. B **98**, 081203(R) (2018).

[33] S. Chae, K. Mengle, J. T. Heron, and E. Kioupakis, Point defects and dopants of boron arsenide from first-principles calculations: Donor compensation and doping asymmetry, Appl. Phys. Lett. **113**, 212101 (2018).

[34] J. S. Kang, M. Li, H. Wu, H. Nguyen, and Y. Hu, Basic physical properties of cubic boron arsenide, Appl. Phys. Lett. **115**, 122103 (2019).

[35] A. Rastogi, P. Rajpoot, and U. P. Verma, Properties of group III–V semiconductor: BAs, Bull. Mater. Sci. **42**, 112 (2019).

[36] J. Jiang, Y. Zhang, C. Chi, Z. Shi, L. Yan, P. Li, B. Zhang, and G. Du, Improved ultraviolet emission performance from polarization-engineered n-ZnO/p-GaN heterojunction diode, Appl. Phys. Lett. **108**, 1897 (2016).

[37] C. Kaewmeechai, Y. Laosiritaworn, and A. P. Jaroenjittichai, DFT band alignment of polar and nonpolar GaN/$MgGeN_2$, ZnO/$MgGeN_2$ and GaN/ZnO heterostructures for optoelectronic device design, Appl. Surf. Sci. **533**, 147503 (2020).

[38] S. Mu, H. Peelaers, Y. Zhang, M. Wang, and C. G. V. de Walle, Orientation-dependent band offsets between $(Al_x\,Ga_{1-x})_2\,O_3$ and $Ga_2\,O_3$, Appl. Phys. Lett. **117**, 252104 (2020).

[39] H. Fu, J. Goodrich, and N. Tansu, Band alignment of ScAlN/GaN heterojunction, Appl. Phys. Lett. **117**, 231105 (2020).

[40] C. G. VandeWalle and R. M. Martin, Theoretical calculations of heterojunction discontinuities in the Si/Ge system, Phys. Rev. B **34**, 5621 (1986).

[41] A. Baldereschi, S. Baroni, and R. Resta, Band Offsets in Lattice-Matched Heterojunctions: A Model and First-Principles Calculations for GaAs/AlAs, Phys. Rev. Lett. **61**, 734 (1988).

[42] K. Zhang, Y. Dai, Z. Zhou, S. Ullah Jan, L. Guo, and J. Ru Gong, Polarization-induced saw-tooth-like potential distribution in zincblende-wurtzite superlattice for efficient charge separation, Nano Energy **41**, 101 (2017).

[43] D. Bai, H. Liu, A. Zhang, J. Wang, G. Tang, J. Zhang, and C. Stampfl, Effect of an Al-adlayer in the c-plane ZnO/AlN heterostructure, Europhys. Lett. **122**, 26003 (2018).

[44] J. Wang, J. Liu, M. Xue, D. Bai, and C. Stampfl, Structural stability and band alignment in the c-plane ZnO/GaN heterostructure, Semicond. Sci. Technol. **34**, 095008 (2019).

[45] J. Castellanos Águila, P. Palacios, J. C. Conesa, J. Arriaga, and P. Wahnón, Electronic band alignment at $CuGaS_2$ chalcopyrite interfaces, Comput. Mater. Sci. **121**, 79 (2016).

[46] K. H. L. Zhang, R. Wu, F. Tang, W. Li, F. E. Oropeza, L. Qiao, V. K. Lazarov, Y. Du, D. J. Payne, J. L. MacManus-Driscoll, and M. G. Blamire, Electronic structure and band alignment at the NiO and $SrTiO_3$ p–n heterojunctions, ACS Appl. Mater. Interfaces **9**, 26549 (2017).

[47] S. Sanna and W. G. Schmidt, GaN/$LiNbO_3$ (0001) interface formation calculated from first-principles, Appl. Surf. Sci. **256**, 5740 (2010).

[48] C. E. Kim, Y. J. Tak, K. T. Butler, A. Walsh, and A. Soon, Lattice-mismatched heteroepitaxy of IV-VI thin films on PbTe(001): An *ab initio* study, Phys. Rev. B **91**, 085307 (2015).

[49] J. L. Du, Y. Fang, E. G. Fu, X. Ding, K. Y. Yu, Y. G. Wang, Y. Q. Wang, J. K. Baldwin, P. P. Wang, and Q. Bai, What determines the interfacial configuration of Nb/Al_2O_3 and Nb/MgO interface, Sci. Rep. **6**, 33931 (2016).

[50] L. Lang, Y.-Y. Zhang, P. Xu, S. Chen, H. J. Xiang, and X. G. Gong, Three-step approach for computing band offsets and its application to inorganic ABX_3 halide perovskites, Phys. Rev. B **92**, 075102 (2015).

[51] A. Franciosi and C. Walle, Heterojunction band offset engineering, Surf. Sci. Rep. **25**, 1 (1996).
[52] X. Fan, B. Chen, M. Zhang, D. Li, Z. Liu, and C. Xiao, First-principles calculations on bonding characteristic and electronic property of TiC (111)/TiN (111) interface, Mater. Des. **112**, 282 (2016).
[53] P. W. Peacock and J. Robertson, Bonding, Energies, and Band Offsets of Si-ZrO_2 and HfO_2 Gate Oxide Interfaces, Phys. Rev. Lett. **92**, 057601 (2004).
[54] J. Robertson and B. Falabretti, Band offsets of high K gate oxides on III-V semiconductors, J. Appl. Phys. **100**, 014111 (2006).
[55] R. Cao, Z. Zhang, C. Wang, H. Li, X. Xie, D. Hong, L. Hui, and W. Wang, Interfacial bonding and electronic structure of GaN/GaAs interface: A first-principles study, J. Appl. Phys **117**, 93 (2015).
[56] R. Marschall, Semiconductor composites: Strategies for enhancing charge carrier separation to improve photocatalytic activity, Adv. Funct. Mater. **24**, 2421 (2014).
[57] P. Zhang, J. Zhang, and J. Gong, Tantalum-based semiconductors for solar water splitting, Chem. Soc. Rev. **43**, 4395 (2014).
[58] W. Feng, Z. Jin, J. Yuan, J. Zhang, S. Jia, L. Dong, J. Yoon, L. Zhou, R. Vajtai, J. M. Tour *et al.*, A fast and zero-biased photodetector based on GaTe–InSe vertical 2d p–n heterojunction, 2D Mater. **5**, 025008 (2018).
[59] C. Liao, Y. Zhao, and G. Ouyang, Strain-modulated band engineering in two-dimensional black phosphorus/MoS_2 van der Waals heterojunction, ACS Omega **3**, 14641 (2018).
[60] J. Shim, S. Oh, D.-H. Kang, S.-H. Jo, M. H. Ali, W.-Y. Choi, K. Heo, J. Jeon, S. Lee, M. Kim *et al.*, Phosphorene/rhenium disulfide heterojunction-based negative differential resistance device for multi-valued logic, Nat. Commun. **7**, 13413 (2016).
[61] R. Yan, S. Fathipour, Y. Han, B. Song, S. Xiao, M. Li, N. Ma, V. Protasenko, D. A. Muller, D. Jena, and H. G. Xing, Esaki diodes in van der Waals heterojunctions with broken-gap energy band alignment, Nano Lett. **15**, 5791 (2015).
[62] L. Dong, H. Sun, J. W. Pomeroy, D. Francis, F. Faili, D. J. Twitchen, and M. Kuball, GaN-on-diamond electronic device reliability: Mechanical and thermo-mechanical integrity, Appl. Phys. Lett. **107**, 151 (2015).
[63] Y. Umeno, A. Kubo, and S. Nagao, Density functional theory calculation of ideal strength of SiC and GaN: Effect of multiaxial stress, Comput. Mater. Sci. **109**, 105 (2015).
[64] H. Xie, Y. Chen, T. Zhang, N. Zhao, and E. Liu, Adhesion, bonding and mechanical properties of Mo doped diamond/Al (Cu) interfaces: A first principles study, Appl. Surf. Sci. **527**, 146817 (2020).
[65] P. E. Blochl, Projector augmented-wave method, Phys. Rev. B **50**, 17953 (1994).
[66] G. K. A and J. Furthmüller, Efficiency of ab-initio total energy calculations for metals and semiconductors using a plane-wave basis set, Comput. Mater. Sci. **6**, 15 (1996).
[67] G. Kresse and J. Furthmuller, Efficient iterative schemes for *ab initio* total-energy calculations using a plane-wave basis set, Phys. Rev. B **54**, 11169 (1996).
[68] P. J. P., B. K., and E. M., Generalized Gradient Approximation Made Simple, Phys. Rev. Lett. **77**, 3865 (1996).
[69] Becke and D. Axel, A new mixing of Hartree–Fock and local density-functional theories, J. Chem. Phys. **98**, 1372 (1993).
[70] J. Heyd, G. E. Scuseria, and M. Ernzerhof, Hybrid functionals based on a screened Coulomb potential, J. Chem. Phys. **124**, 219906 (2006).
[71] A. V. Krukau, O. A. Vydrov, A. F. Izmaylov, and G. E. Scuseria, Influence of the exchange screening parameter on the performance of screened hybrid functionals, J. Chem. Phys. **125**, 224106 (2006).
[72] C. Adamo and V. Barone, Toward reliable density functional methods without adjustable parameters: The PBE0 model, J. Chem. Phys. **110**, 6158 (1999).
[73] K. Luo, Q. Deng, X. Zha, Q. Huang, J. S. Francisco, X. Yu, Y. Qiao, J. He, and S. Du, Electronic structures and mechanical properties of Al(111)/ZrB_2(0001) heterojunctions from first-principles calculation, Mol. Phys. **113**, 1794 (2015).
[74] D. Yin, X. Peng, Q. Yi, and Z. Wang, Impact of residual stress on the adhesion and tensile fracture of TiN/CrN multi-layered coatings from first principles, Physica E: Low Dimens. Syst. Nanostruct. **44**, 1838 (2012).
[75] See Supplemental Material at http://link.aps.org/supplemental/10.1103/PhysRevMaterials.6.034603 for more information on: (1) twelve tested equilibrium structures of BAs/GaN heterojunction interfaces; (2) the comparison of the planar average of electrostatic potentials calculated with PBE and HSE; (3) the energy-strain curves of BAs/GaN heterojunctions; (4) the comparison of the deformation potential with and without pseudohydrogen; (5) the calculated Elastic constants C_{ij} and Poisson's ratio ν_{ij} of bulks and BAs/GaN heterojunctions; and (6) the density of states on each layer for the BAs/GaN heterojunctions and superlattices.
[76] B. Li, H. Sun, and C. Chen, Large indentation strain-stiffening in nanotwinned cubic boron nitride, Nat. Commun. **5**, 4965 (2014).
[77] B. Li, H. Sun, and C. Chen, Extreme Mechanics of Probing the Ultimate Strength of Nanotwinned Diamond, Phys. Rev. Lett. **117**, 116103 (2016).
[78] R. M. Martin, *Electronic structure: Basic theory and practical methods* (Cambridge University Press, Cambridge, 2020).
[79] Q. Peng, Z. Wang, B. Sa, B. Wu, and Z. Sun, Blue phosphorene/MS_2 (M = Nb, Ta) heterostructures as promising flexible anodes for lithium-ion batteries, ACS Appl. Mater. Interfaces **8**, 13449 (2016).
[80] Q. Wei and X. Peng, Superior mechanical flexibility of phosphorene and few-layer black phosphorus, Appl. Phys. Lett. **104**, 372 (2014).
[81] L. Weston, H. Tailor, K. Krishnaswamy, L. Bjaalie, and C. Van de Walle, Accurate and efficient band-offset calculations from density functional theory, Comput. Mater. Sci. **151**, 174 (2018).
[82] R. Ahmed, S. Javad Hashemifar, H. Akbarzadeh, M. Ahmed, and F. Aleem, *Ab initio* study of structural and electronic properties of III-arsenide binary compounds, Comput. Mater. Sci. **39**, 580 (2007).
[83] S. Lyu and A. Pasquarello, Band alignment at β-Ga_2O_3/III-N (III = Al, Ga) interfaces through hybrid functional calculations, Appl. Phys. Lett. **117**, 102103 (2020).
[84] M. Yamaguchi, T. Yagi, T. Sota, T. Deguchi, and S. Nakamura, Brillouin scattering study of bulk GaN, J. Appl. Phys. **85**, 8502 (1999).
[85] Z. Zhang, R. Cao, C. Wang, H. B. Li, H. Dong, W. H. Wang, F. Lu, Y. Cheng, X. Xie, and H. Liu, GaN as an interfacial

passivation layer: Tuning band offset and removing fermi level pinning for III–V MOS devices, ACS Appl. Mater. Interfaces **7**, 5141 (2015).

[86] W. Lv, L. Yan, X. Pang, H. Yang, L. Qiao, Y. Su, and K. Gao, Study of the stability of α-Fe/MnS interfaces from first principles and experiment, Appl. Surf. Sci. **501**, 144017.1 (2020).

[87] X. Yuan, Yuan, Y. Xiao, G. Wang, and L. Zhang, TiN inducing ferrite nucleation based on the bcc-Fe/TiN interfaces formation at atomic scale by first-principles calculation, Comput. Mater. Sci. **197**, 110570 (2021).

[88] Y. Liu, J.-C. Wen, X.-Y. Zhang, and Y.-C. Huang, A comparative study on heterogeneous nucleation and mechanical properties of the fcc-Al/$L1_2$-Al_3M (M = Sc, Ti, V, Y, Zr, Nb) interface from first-principles calculations, Phys. Chem. Chem. Phys. **23**, 4718 (2021).

[89] J. Zhang, Y. Zhang, K. Tse, and J. Zhu, Hydrogen surfactant assisted coherent growth of GaN on ZnO substrate, Phys. Rev. Mater. **2**, 013403 (2018).

[90] T. Akiyama, H. Nakane, K. Nakamura, and T. Ito, Effective approach for accurately calculating individual energy of polar heterojunction interfaces, Phys. Rev. B **94**, 115302 (2016).

[91] J. Zhang, Y. Zhang, K. Tse, B. Deng, H. Xu, and J. Zhu, New approaches for calculating absolute surface energies of wurtzite (0001)/(0001): A study of ZnO and GaN, J. Appl. Phys. **119**, 449 (2016).

[92] Y. Zhang, J. Zhang, K. Tse, L. Wong, C. Chan, B. Deng, and J. Zhu, Pseudo-hydrogen passivation: A novel way to calculate absolute surface energy of zinc blende (111)/($\bar{1}\bar{1}\bar{1}$) surface, Sci. Rep. **6**, 20055 (2016).

[93] D. M. Lipkin, D. R. Clarke, and A. G. Evans, Effect of interfacial carbon on adhesion and toughness of gold-sapphire interfaces, Acta Mater. **46**, 4835 (1998).

[94] W. Guo, H. Xu, L. Chen, H. Yu, and J. Ye, Polarity control and fabrication of lateral-polarity-structure of III-nitride thin films and devices: progress and prospect, J. Phys. D: Appl. Phys. **53**, 483002 (2020).

[95] H. Wang, L. Zhang, Z. Chen, J. Hu, S. Li, Z. Wang, J. Liu, and X. Wang, Semiconductor heterojunction photocatalysts: Design, construction, and photocatalytic performances, Chem. Soc. Rev. **43**, 5234 (2014).

[96] M. A. Steiner, R. M. France, J. Buencuerpo, J. F. Geisz, M. P. Nielsen, A. Pusch, W. J. Olavarria, M. Young, and N. J. Ekins-Daukes, High efficiency inverted GaAs and GaInP/GaAs solar cells with strain-balanced GaInAs/GaAsP quantum wells, Adv. Energy Mater. **11**, 2002874 (2021).

[97] X. Ren, J. Li, D. Gao, L. Wu, and G. Pei, Analysis of a novel photovoltaic/thermal system using InGaN/GaN MQWs cells in high temperature applications, Renew. Energy **168**, 11 (2021).

[98] C. C. Loo, S. S. Ng, and W. S. Chang, Photostrictive behavior as the piezo-phototronic effect in InGaN/GaN multiple quantum wells, Nano Energy **86**, 106085 (2021).

[99] A. Khan, K. Balakrishnan, and T. Katona, Ultraviolet light-emitting diodes based on group three nitrides, Nat. Photonics **2**, 77 (2008).

[100] V. Letka, A. P. Craig, A. Bainbridge, and A. R. J. Marshall, A superlattice-based resonant cavity-enhanced photodetector operating in the long-wavelength infrared, Appl. Phys. Lett. **117**, 073503 (2020).